The Astrophysical Journal, 941:103 (19pp), 2022 December 20 https://doi.org/10.3847/1538-4357/ac8c92

A Mechanistic Study on the Formation of Acetone (CH_3COCH_3), Propanal (CH_3CH_2CHO), Propylene Oxide (*c*-CH_3CHOCH_2) along with Their Propenol Enols ($CH_3CHCHOH$/$CH_3C(OH)CH_2$) in Interstellar Analog Ices

Santosh K. Singh[1,2], N. Fabian Kleimeier[1,2], André K. Eckhardt[3], and Ralf I. Kaiser[1,2]

[1] Department of Chemistry, University of Hawaii at Manoa, Honolulu, HI, 96822, USA; ralfk@hawaii.edu

[2] W. M. Keck Research Laboratory in Astrochemistry, University of Hawaii at Manoa, Honolulu, HI, 96822, USA

[3] Lehrstuhl für Organische Chemie II, Ruhr-Universität Bochum, D-44801 Bochum, Germany; Andre.Eckhardt@rub.de

Received 2022 May 3; revised 2022 August 16; accepted 2022 August 23; published 2022 December 15

Abstract

Carbonyl-bearing complex organic molecules (COMs) in the interstellar medium (ISM) are of significant importance due to their role as potential precursors to biomolecules. Simple aldehydes and ketones like acetaldehyde, acetone, and propanal have been recognized as fundamental molecular building blocks and tracers of chemical processes involved in the formation of distinct COMs in molecular clouds and star-forming regions. Although previous laboratory simulation experiments and modeling established the potential formation pathways of interstellar acetaldehyde and propanal, the underlying formation routes to the simplest ketone—acetone—in the ISM are still elusive. Herein, we performed a systematic study to unravel the synthesis of acetone, its propanal and propylene oxide isomers, as well as the propenol tautomers in interstellar analog ices composed of methane and acetaldehyde along with isotopic-substitution studies to trace the reaction pathways of the reactive intermediates. Chemical processes in the ices were triggered at 5.0 K upon exposure to proxies of Galactic cosmic rays in the form of energetic electrons. The products were detected isomer-selectively via vacuum ultraviolet (VUV) photoionization reflectron time-of-flight mass spectrometry. In our experiments, the branching ratio of acetone (CH_3COCH_3):propylene oxide (*c*-CH_3CHOCH_2):propanal (CH_3CH_2CHO) was determined to be (4.82 ± 0.05):(2.86 ± 0.13):1. The radical–radical recombination reaction leading to acetone emerged as the dominant channel. The propenols appeared only at a higher radiation dose via keto–enol tautomerization. The current study provides mechanistic information on the fundamental nonequilibrium pathways that may be responsible for the formation of acetone and its (enol) isomers inside the interstellar icy grains.

Unified Astronomy Thesaurus concepts: Interstellar medium (847); Mass spectrometry (2094); Interstellar molecules (849)

1. Introduction

Over the last decade, the untangling of the formation mechanisms of molecules carrying the carbonyl (C=O) moiety, such as acetic acid (CH_3COOH), methyl formate ($HCOOCH_3$), formic acid (HCOOH), acetaldehyde (CH_3CHO), glycolaldehyde ($HOCH_2CHO$), glyoxylic acid (HCOCOOH), and pyruvic acid ($CH_3COCOOH$) in the interstellar medium (ISM) has gained considerable interest in the astrochemistry and astrobiology communities (Bennett & Kaiser 2007a, 2007b; Bennett et al. 2007; Halfen et al. 2011; Kleimeier et al. 2020b, 2021b). This attention is due to the role of these molecules as potential precursors to complex biomolecules such as carbohydrates (Bennett & Kaiser 2007b; Jalbout 2008; Kleimeier et al. 2021b) amino acids (Kuan et al. 2003; Holtom et al. 2005), and polypeptides (Halfen et al. 2011; Förstel et al. 2016; Frigge et al. 2018a) relevant to the origin of life (Kuan et al. 2003; Jalbout 2008). Since the discovery toward the hot molecular core Sagittarius (Sgr) B2 (N-LHM) (Combes et al. 1987; Snyder et al. 2002) and in the Orion-BN/KL star-forming region, acetone (CH_3COCH_3)—the simplest representative of a ketone—has been recognized as an excellent tracer for elucidating the effects of physical and chemical conditions on the formation of distinct complex organic molecules (COMs) in molecular clouds and star-forming regions (Peng et al. 2013; Andrade et al. 2014). Peng et al. suggest that the difference in the distribution of acetone (CH_3COCH_3) relative to other large N- and O-bearing molecules in the Orion-BN/KL region makes acetone a tool to test different astrochemical models of complex molecules. A radiative decomposition study of acetone reveals that the former molecule could be a potential source of interstellar ketene (H_2CCO) (Hudson 2018). Two structural isomers of acetone (CH_3COCH_3)—the aldehyde propanal (CH_3CH_2CHO) and the chiral epoxide propylene oxide (*c*-CH_3CHOCH_2)—were also detected toward Sgr B2 (N) (Hollis et al. 2004; McGuire et al. 2016). However, the underlying routes of acetone in these interstellar environments have not been fully explored.

Previously proposed gas-phase ion–molecule radiative associations such as $CH_3^+ + CH_3CHO \rightarrow (CH_3)_2CHO^+$ followed by dissociative electron–ion recombination (Combes et al. 1987) cannot account for the observed fractional abundances of acetone (CH_3COCH_3) toward Sgr B2 (Herbst et al. 1990). Garrod et al. proposed an extended grain-surface model, in which acetone is speculated to be formed by the radical–radical recombination of methyl ($\cdot CH_3$) and acetyl ($CH_3\dot{C}O$) radicals on grain surfaces (Garrod et al. 2008). However, this model also fails to explain the observed abundances of acetone since only grain-surface reactions were included, but the bulk ice chemistry was ignored (Peng et al. 2013). The discrepancies between modeled and observed abundances are likely due to the fact that current astronomical models fail to include the chemical processing of the icy mantle of interstellar grains by ionizing radiation. The critical effect of the ice mantle in the formation of COMs has been documented recently by Kleimeier et al. (2021a), Bergantini et al. (2018a), and Abplanalp et al. (2016) to explain the astronomical detection of cyclopropenone (c-C_3H_2O), propylene oxide (c-CH_3CHOCH_2), and the isomer pair acetaldehyde (CH_3CHO)/vinyl alcohol (C_2H_3OH). The ice mantle on interstellar grains with typical thicknesses of a few hundred nanometers consists of small molecules such as water (H_2O), ammonia (NH_3), methane (CH_4), carbon dioxide (CO_2), carbon monoxide (CO), and methanol (CH_3OH) (Schutte & Ehrenfreund 2000; Gibb et al. 2000, 2004). The interaction of these ices with galactic cosmic rays (GCRs) and ultraviolet photons generates reactive radical species; these radicals are generated under conditions that are not in thermodynamic equilibrium with the surrounding ice environment (Kaiser & Roessler 1997; Bisschop et al. 2007; Garozzo et al. 2010; Turner & Kaiser 2020) with suprathermal atoms and radicals eventually forming COMs within "bulk" ices at 10 K. As dense molecular clouds undergo gravitational collapse and transform into star-forming regions, the rise in temperature up to 250–300 K partially sublimes the synthesized COMs from grains into the gas phase, where they can be detected by radio telescopes. Previous experimental and simulation studies indicate that the majority of COMs are likely formed on icy mantle-coated interstellar grains (Bernstein et al. 1995; Herbst 2014; Boogert et al. 2015; Förstel et al. 2017; Bergantini et al. 2018b; Frigge et al. 2018b; Zhu et al. 2018b; Abplanalp & Kaiser 2019; Arumainayagam et al. 2019; Eckhardt et al. 2019; Turner & Kaiser 2020).

Exploiting interstellar model ices, it has been revealed that acetone can form in the ice mixtures containing carbon monoxide (CO), methane (CH_4), and methanol (CH_3OH) (Kaiser et al. 2014; Maity et al. 2015; Abplanalp et al. 2016) upon exposure to ionizing radiation. The initial steps of the reaction most likely involve the barrierless radical–radical recombination of methyl ($\cdot CH_3$) and formyl ($H\dot{C}O$) radicals to form acetaldehyde (CH_3CHO), provided the reactants have a proper geometrical orientation for recombination. The acetaldehyde molecule (CH_3CHO) may release a hydrogen atom to form an acetyl radical ($CH_3\dot{C}O$) (Feldman et al. 2001; Kleimeier et al. 2020c), which can combine with a methyl radical ($\cdot CH_3$) to form acetone (CH_3COCH_3)—once again if both the reactants have a favorable recombination geometry. However, mechanistic evidence of this multistep sequence to acetone (CH_3COCH_3) is still lacking. Alternatively, acetaldehyde (CH_3CHO) could dissociate to form a vinoxy radical ($\cdot CH_2CHO$) (Swiderek et al. 2007), which upon interaction with the methyl radical ($\cdot CH_3$) will generate propanal (CH_3CH_2CHO). Thus, the interplay between these two potential reaction channels will govern the extent to which acetone and/or propanal are formed in the ices. For instance, both propanal (CH_3CH_2CHO) and acetone (CH_3COCH_3) have been observed in processed CO–CH_4 ices (Abplanalp & Kaiser 2019), with the former being the major product, while only propanal is observed in CO–CH_3CH_3 ice mixture (Abplanalp et al. 2016). Once again, despite the explicit identification of both isomers, distinct reaction pathways are still elusive. Yet another possible route to interstellar acetone (CH_3COCH_3) involves the interaction of excited singlet oxygen ($O(^1D)$) with propylene (C_3H_6); this reaction also accesses propanal (CH_3CH_2CHO) and primarily propylene oxide (c-CH_3CHOCH_2) (Bergantini et al. 2018a). The vacuum ultraviolet (VUV) photolysis study of the CH_4+O_2 ice mixture revealed a new IR absorption feature at 1722 cm^{-1}, which was assigned to C_3H_6O (acetone); however, the assignment was not confirmed through mass spectrometric techniques (Chou et al. 2020).

Here, we investigated the synthesis of acetone (CH_3COCH_3), its propanal (CH_3CH_2CHO) and propylene oxide (c-CH_3CHOCH_2) isomers, as well as the propenol tautomers ($CH_3CHCHOH$, $CH_3C(OH)CH_2$) in interstellar analog ices comprising methane (CH_4) and acetaldehyde (CH_3CHO). The acetaldehyde molecule has been recognized as a precursor of carbonyl bearing COMs such as acetic acid (Kleimeier et al. 2020a), pyruvic acid (Kleimeier et al. 2020b), and diketone 2,3-butanedione (Kleimeier et al. 2020c) in interstellar analog ices. In the gas phase, acetaldehyde (CH_3CHO) has been detected in cold molecular clouds of TMC-1 (Matthews et al. 1985), in warmer envelopes around star-forming region Sgr B2 (Fourikis et al. 1974), toward hot cores of NGC 6334F (Nummelin et al. 1998), in the Murchison meteorite (Jungclaus et al. 1976), and in comets such as Hale–Bopp (Crovisier et al. 2004). Furthermore, tentative detections of acetaldehyde in interstellar ices have been reported with upper limits of 10% relative to water (Gibb et al. 2004). Thus, ices containing acetaldehyde and methane can be regarded as polar interstellar model ices. The chemical processing of these ices is triggered at 5 K upon exposure to energetic electrons. These electrons mimic the secondary electrons generated in the path of the galactic cosmic rays once penetrating the interstellar ices (Bennett et al. 2005). Isotopic-substitution experiments to the CD_4–CH_3CHO system at low doses are conducted to trace the reaction pathways unambiguously. The structural isomers are deciphered isomer-selectively through single photon photoionization reflectron time-of-flight mass spectrometry (PI-ReTOF-MS) (Frigge et al. 2018a; Zhu et al. 2018a; Turner & Kaiser 2020; Singh & Kaiser 2021). This method selectively ionizes isomers during the sublimation phase of the processed ice and identifies them based on their ionization energies; therefore, since different isomers have distinct ionization energies and ideally discrete sublimation temperatures, structural isomers can be detected, thus providing fundamental mechanistic information on the chemical processes that may be involved in the formation of interstellar acetone (CH_3COCH_3) along with its isomers at temperatures as low as 10 K inside interstellar icy grains.

2. Methods

2.1. Experimental

Taking into account the molecular structure and the ionization energies of acetone along with its isomers (Figure 1 and Table 1), ice mixtures of methane (CH_4)–acetaldehyde (CH_3CHO) and d_4-methane (CD_4)–acetaldehyde (CH_3CHO) were explored. The choice of d_4-methane (CD_4) in isotopic experiments assists in the elucidation of distinct reaction pathways based on mass shifts and the emergence of products of different mass-to-charge (m/z) ratios, as detailed in Figures 2(a) and (b). In principle, upon interaction with ionizing radiation, acetaldehyde (CH_3CHO; 44 amu) can lose a hydrogen atom from the formyl moiety or from the methyl group forming the acetyl ($CH_3\dot{C}O$; 43 amu) and vinoxy ($\cdot CH_2CHO$; 43 amu) radical fragments, respectively (Figure 2(a)). Upon interaction with ionizing radiation, d_4-methane generates a d_3-methyl radical ($\cdot CD_3$; 18 amu) via a deuterium loss or d_2-methylene ($:CD_2$; 16 amu) via loss of molecular deuterium (Kaiser et al. 2014; Maity et al. 2014a; Abplanalp et al. 2018, 2019; Zhu et al. 2018b). The barrierless radical–radical reaction of the d_3-methyl radical ($\cdot CD_3$; 18 amu) with acetyl ($CH_3\dot{C}O$;

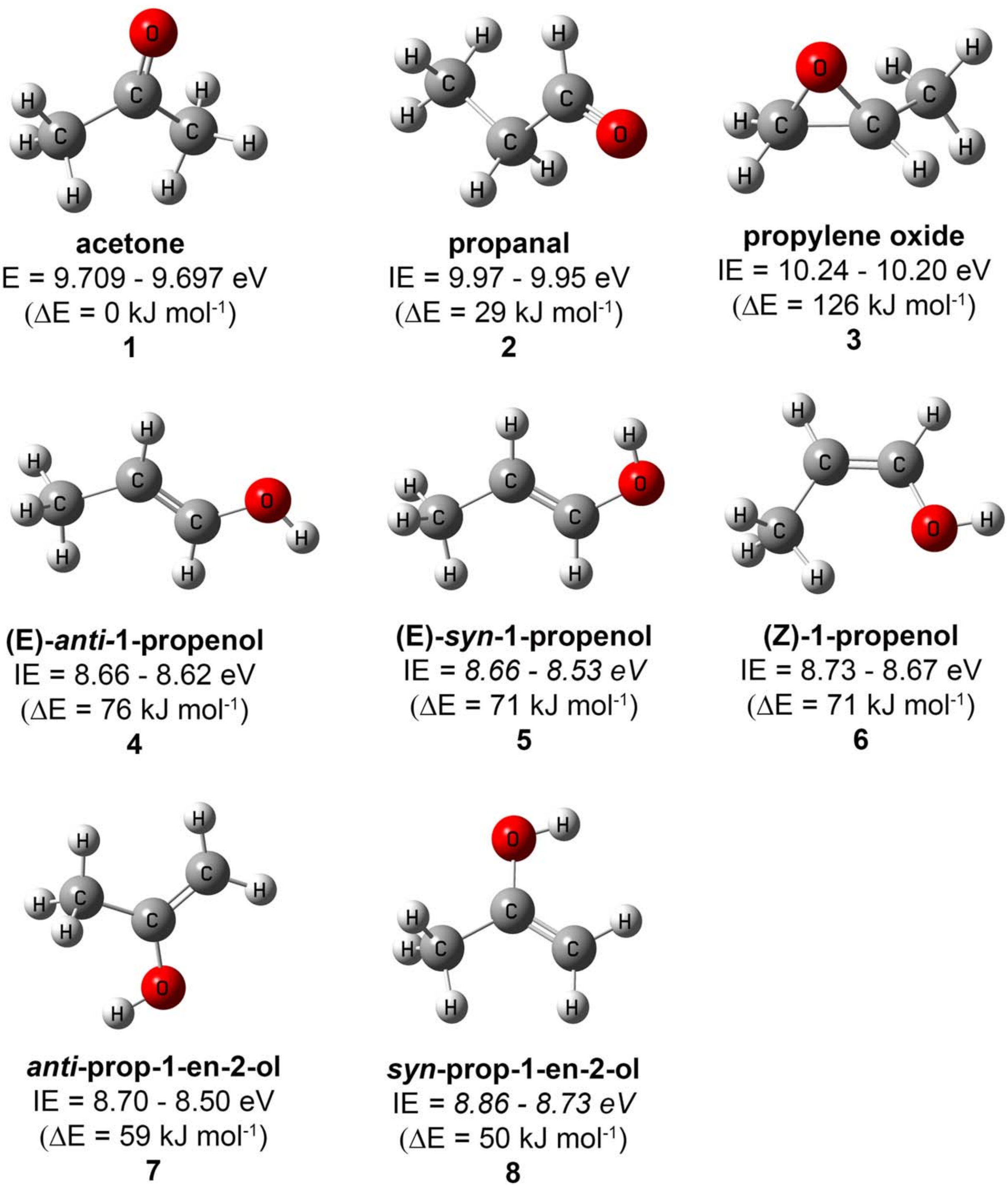

Figure 1. Molecular structures of C_3H_6O isomers along with their experimental adiabatic IE range in eV and calculated relative energies (ΔE) in kJ mol^{-1}. For isomers 5 and 8, calculated IEs (in italics) incorporating the error range are provided Table 1). The experimental adiabatic IEs are obtained from the NIST database.

43 amu) and vinoxy ($\cdot CH_2CHO$; 43 amu) can generate d_3-acetone (CD_3COCH_3; 61 amu) and d_3-propanal (CD_3CH_2CHO; 61 amu) respectively, which then can be distinguished based on their adiabatic ionization energies of 9.703 ± 0.006 eV and 9.96 ± 0.01 eV, respectively. On the other hand, the reaction of acetaldehyde (CH_3CHO; 44 amu) with d_2-methylene ($:CD_2$; 16 amu) can proceed via four channels leading through the insertion and addition to products of 60 amu. The insertion may form 1,1-d_2-propanal (CD_2HCH_2CHO), 2,2-d_2-propanal (CH_3CD_2CHO), and 1,1-d_2-acetone (CD_2HCOCH_3), whereas the addition to the carbonyl functional group could yield d_2-propylene oxide (c-CH_3CHOCD_2). Thus, radical–radical recombination and the carbene reaction pathways can be discriminated based on the appearance of the product signal at mass-to-charge ratios of 61 versus 60, respectively. The products formed at $m/z = 60$ can then be discriminated based on their distinct ionization energies as compiled in Figure 2(a). Extended irradiation times and hence higher doses can lead to keto–enol tautomerization as higher-generation products (Abplanalp et al. 2016; Kleimeier et al. 2021b; Kleimeier & Kaiser 2021; Singh et al. 2021). In the case of acetone (CH_3COCH_3; 58 amu) and propanal (CH_3CH_2CHO; 58 amu) (Figure 2(b)), this tautomerization can lead to 2-propenols and

Table 1
Experimental and calculated adiabatic ionization energies of C_3H_6O isomers

	Name	IE (eV) Comp.	IE (eV) Exp.[a]	IE (Comp. - Exp.) Upper limit	IE (Comp. - Exp) Lower limit	IE range[b]
1	propanal	9.94	9.96 ± 0.01	−0.03	−0.01	–
2	acetone	9.67	9.703 ± 0.006	−0.036	−0.024	–
3	propylene oxide	10.10	10.22 ± 0.02	−0.14	−0.10	
4	(*E*)-*anti*−1-propenol	8.64	8.64 ± 0.02	−0.02	0.02	–
5	(*E*)-*syn*−1-propenol	8.60	–	–	–	8.66–8.53
6	(*Z*)−1-propenol	8.70	8.70 ± 0.03	−0.03	0.03	–
7	*anti*-prop-1-en-2-ol	8.67	8.60 ± 0.10	−0.03	0.07	–
8	*syn*-prop-1-en-2-ol	8.80	–	–	–	8.86–8.73
			Average	−0.05 ± 0.04	−0.01 ± 0.05	
			Error limits	Combined error limits −0.09 to +0.04		

Notes.
[a] Values from NIST database.
[b] IE range is determined by including the error limits in the calculated IE and subtracting 0.03 eV to include the stark effect.

1-propenols, respectively (Figures 1 and 2(b)). These enols have lower-ionization energies than the corresponding ketone (acetone) and aldehyde (propanal) and hence can be discriminated by conducting experiments at distinct photon energies.

The experiments were conducted in an ultrahigh vacuum (UHV) chamber evacuated to a base pressure of a few 10^{-11} Torr using turbo-molecular pumps backed by a dry scroll pump (Bennett et al. 2013; Jones & Kaiser 2013). A polished silver substrate was mounted on a cold finger, which can be freely rotated in a horizontal plane using a doubly differentially pumped rotational feedthrough and translated vertically via a movable UHV compatible bellow. The substrate temperature was maintained at 5.0 ± 0.2 K using a closed-cycle helium refrigerator (Sumitomo Heavy Industries, RDK-415E). Acetaldehyde (CH_3CHO; >99.5% purity, Sigma Aldrich, p. a., anhydrous) was stored in a glass vial interfaced to a UHV chamber and subjected to six freeze–pump–thaw cycles to remove the dissolved atmospheric gases. Acetaldehyde vapor and d_4-methane (CD_4; 99.8% purity, Sigma Aldrich) gases were codeposited via separate glass capillary arrays onto the cold silver substrate maintained at 5.0 ± 0.2 K to form the ice mixtures. During the deposition, the partial pressures of d_4-methane (CD_4) and acetaldehyde were maintained at 1×10^{-9} torr and 2×10^{-8} torr, respectively. The nonisotopic experiments were performed with the ice mixtures of acetaldehyde (CH_3CHO) and methane (CH_4). The thickness of each ice was monitored in situ using laser interferometry. In this technique, a He–Ne laser of 632.8 nm wavelength was incident on the silver substrate at an angle of 4°, and the intensity of the reflected light was measured using a photodiode (Turner et al. 2015). The interference pattern formed after the reflection of the laser light from the silver substrate and ice surface was recorded. Three interference fringes were observed during the deposition of the ice. Using the average refractive index of the ice mixture ($n_{ice} = 1.32$) determined from the refractive indices of the neat methane ($n = 1.28$) (Gerakines & Hudson 2015) and acetaldehyde ices ($n = 1.303$) (Hudson & Coleman 2019), the thicknesses of the ices were determined to be 720 ± 50 nm.

The infrared spectra of the ice mixtures were collected in the 4000–700 cm^{-1} region using a Fourier Transform Infrared Spectrometer (FTIR; Nicolet 6700) operated at a resolution of 4 cm^{-1} in an absorption–reflection–absorption mode with an incidence angle of 45°. In order to derive the relative amount of each component for the binary mixture, the column densities of methane (CH_4) and acetaldehyde (CH_3CHO) were calculated by applying the absorptions coefficients of 1.04×10^{-17} and 1.9×10^{-18} cm $molecule^{-1}$ (Gerakines & Hudson 2015; Kleimeier et al. 2020a) to the integrated areas of their respective bands at 1303 cm^{-1} (ν_4; CH_4) and 1428 cm^{-1} (ν_5; CH_3CHO) in a modified Lambert–Beer equation (Bennett et al. 2004). Based on the column densities, the ratio of methane (CH_4): acetaldehyde (CH_3CHO) in the ice mixture was found to be 1.13 ± 0.2:1. Thereafter, each ice mixture was exposed to 5 keV energetic electrons at an electron current of 15 ± 2 nA for 5 minutes. High-dose experiments with an electron current of 100 ± 10 nA for 10 minutes were performed only for the nonisotopic ice (CH_4–CH_3CHO) mixture to facilitate the formation of enols. FTIR spectra of the ices were measured in situ during irradiation to monitor the changes induced by the ionizing radiation. Using Monte Carlo simulations via CASINO 2.42 software (Drouin et al. 2007), the average energy dose at an irradiation current of 15 ± 2 nA for 5 minutes was calculated to be 0.30 ± 0.03 eV $molecule^{-1}$ for acetaldehyde (CH_3CHO) and 0.11 ± 0.01 eV $molecule^{-1}$ for d_4-methane (Table 2). At the high irradiation current (100 ± 10 nA for 10 minutes), the average energy doses for acetaldehyde and methane are 4.1 ± 0.4 eV $molecule^{-1}$ and 1.5 ± 0.1 eV $molecule^{-1}$. Hereafter, ices were annealed at a rate of 1 K $minute^{-1}$, and molecules subliming from the substrate were ionized and detected using PI-ReTOF-MS. The tunable pulsed VUV lights for photoionization were generated via a resonant four-wave mixing technique. In this technique, the fundamental and doubled/tripled output of two separate dye lasers (Sirah, Cobra-Stretch) pumped by two Nd:YAG lasers (Spectra-Physics, Quanta Ray Pro 250-30; 30 Hz) were spatially and temporally overlapped inside the pulsed jet of krypton or xenon to generate the VUV light. Dye lasers were tuned to generate the VUV lights of the desired wavelength (Table 3). A biconvex lithium fluoride (LiF) lens in an off-axis geometry was utilized to separate the VUV light from the residual dye beams. The separated VUV light passes through the ceramic aperture (1 mm) and is directed at about 2 mm above the sample to ionize the subliming molecules. The ions formed were extracted and eventually separated based on their mass-to-charge (m/z) ratio before reaching the microchannel plate (MCP) detector. The MCP detector generates a signal when ions reach the detector. This signal is amplified using a preamplifier (Ortec 9305) and shaped with a 100 MHz discriminator. The discriminator sends the signal to a computer-based

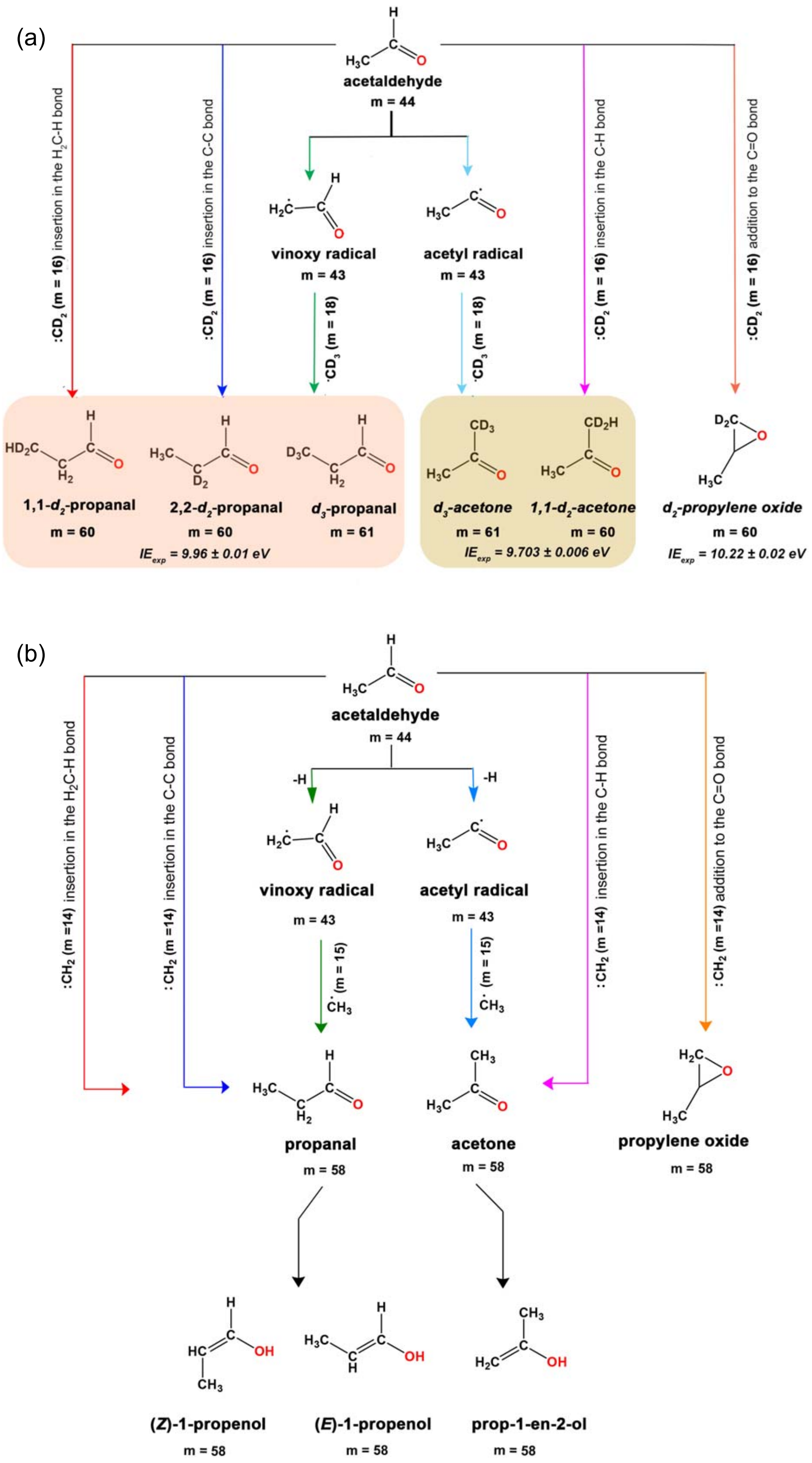

Figure 2. (a) Reaction scheme depicting the reaction channels leading to distinct first-generation products acetone, propanal, and propylene oxide in irradiated CD_4–CH_3CHO ices. Radical–radical recombination reactions of vinoxy and acetyl radicals with d_3-methyl radical are indicated by green and light-blue-colored arrows. The insertion of d_2-carbene in the H_2C–H, C–C, and C–H bonds of acetaldehyde are indicated by red-, blue-, and pink-colored arrows, respectively. The orange-colored arrow indicates the addition reaction of d_2-carbene to the C=O bond of acetaldehyde. The deuterated positional isomers of propanal and acetone are grouped into separate red and green colored boxes for clarity. (b) Reaction scheme depicting the reaction channels leading to acetone, propanal, and propylene oxide along with their enols in irradiated CH_4–CH_3CHO ices. Radical–radical recombination reactions of vinoxy and acetyl radicals with methyl radical are indicated by green- and light-blue-colored arrows, respectively. Carbene insertion at the H_2C–H, C–C, and C–H bonds of acetaldehyde are indicated by red-, blue-, and pink-colored arrows, respectively. The orange-colored arrow indicates the addition reaction of carbene to the C=O bond of acetaldehyde.

Table 2
Data Applied to Calculate the Average Dose per Molecule in (CD_4 + CH_3CHO) and (CH_4 + CH_3CHO) Ice Mixtures

	CD_4 + CH_3CHO	CH_4 + CH_3CHO
Initial kinetic energy of the electrons	5 keV	5 keV
Irradiation current, (I)	15 ± 2 nA	100 ± 10 nA
Irradiation time (t)	300 s	600 s
Average penetration depth (l)	424 ± 40 nm	424 ± 40 nm
Average kinetic energy of backscattered electrons (E_{bs}[a])	3.0 ± 0.3 keV	3.0 ± 0.3 keV
Fraction of backscattered electrons (f_{bs}[a])	0.38 ± 0.04	0.38 ± 0.04
Average kinetic energy of transmitted electrons (E_{trans}[a])	0.0 keV	0.0 keV
Fraction of transmitted electrons (f_{trans}[a])	0	0
Average density of the ice mixture (ρ)	0.72 g cm^{-3}	0.62 g cm^{-3}
Irradiated area (A)	1.0 ± 0.2 cm^2	1.0 ± 0.2 cm^2
Total number of molecules processed	(9.8 ± 1.0) × 10^{17}	(9.8 ± 1.0) × 10^{17}
Dose per molecule (D)	acetaldehyde: 0.30 ± 0.03 eV d_4-methane: 0.11 ± 0.01 eV	acetaldehyde: 4.06 ± 0.4 eV methane: 1.48 ± 0.1 eV
Total number of electrons	(2.8 ± 0.3) × 10^{13}	(3.7 ± 0.4) × 10^{14}

Note.
[a] Values from CASINO simulations.

Table 3
Parameters for the Vacuum Ultraviolet (VUV) Light Generated in the Present Study

Photon Energy (eV)		10.49	10.11	9.80	9.20	8.40
$3\omega_1$	Wavelength (nm)	118.19	⋯	⋯	⋯	⋯
$2\omega_1$-ω_2	Wavelength (nm)	⋯	122.63	126.51	134.76	147.60
ω_1	Wavelength (nm)	355	202.316	202.316	222.566	249.628
Nd:YAG (ω_1)	Wavelength (nm)	355	532	532	355	355
Dye laser (ω_1)	Wavelength (nm)	⋯	606.948	606.948	445.132	499.256
Dye		⋯	Rh 610/ Rh 640	Rh 610/ Rh 640	Coumarin 450	Coumarin 503
ω_2	Wavelength (nm)	⋯	577.619	504.725	637.7	808.482
Nd:YAG (ω_2)	Wavelength (nm)	⋯	532	355	532	532
Dye laser (ω_2)	Wavelength (nm)	⋯	577.619	504.725	637.7	808.482
Dye		⋯	Pyrromethane 597	Coumarin 503	DCM	LDS 821
	Nonlinear medium	Xe	Kr	Kr	Xe	Xe

multichannel scaler, which records the signal in 4 ns bins triggered at 30 Hz by a pulsed delay generator. Three thousand six hundred sweeps were collected for each mass spectrum per 1 K increase in the temperature during the temperature-programmed desorption (TPD) phase.

2.2. Computational

All computations were carried out using Gaussian 16, Revision A.03 (Frisch et al. 2016). Geometry and frequency calculations of possible C_3H_6O isomers were performed employing the B3LYP functional (Becke 1988; Lee et al. 1988) with the Dunning correlation-consistent split valence basis set (cc-pVTZ) (Dunning 1989). For higher accuracy, their CCSD(T)/cc-pVDZ, CCSD(T)/cc-pVTZ, and CCSD(T)/cc-pVQZ single-point energies were calculated and extrapolated to the complete basis set limit (Peterson et al. 1994) CCSD(T)/CBS, with B3LYP/cc-pVTZ zero-point vibrational energy (ZPVE) corrections. The adiabatic ionization energies were computed by taking the ZPVE-corrected energy difference between the neutral and ionic species that correspond to similar conformations. The difference between deuterated and nondeuterated isotopologues in the zero-point vibrational energy is marginal; therefore, we used the ZPVEs of nondeuterated isotopologues for ionization energies (IEs) calculation and assumed them to be the same for our experiments with heavier isotopologues. Calculations performed for a small subset of the molecules using the computationally more expensive augmented basis sets at the same zeta level revealed that they did not affect the ionization energies to the significant figures reported and only had a marginal effect on the relative energies of less than 2 kJ mol^{-1}.

3. Results and Discussion

3.1. IR Spectroscopy

The FTIR spectra of the CD_4–CH_3CHO ice mixture before and after the irradiation at a low dose are depicted in Figure 3(a). Fundamental vibrations of acetaldehyde such as the CH_3 symmetric stretch (ν_{11}), the C–H (ν_3) and C=O (ν_4) stretches of the formyl group, and the CH_3 deformation (ν_5) appear at 2922, 2751, 1726, and 1424 cm^{-1}, respectively. Prominent absorption features of d_4-methane are observed at 2250 (ν_3; CD_4 asymmetric stretch), 2109 (ν_1; CD_4 symmetric stretch), and 997 (ν_4; C–D

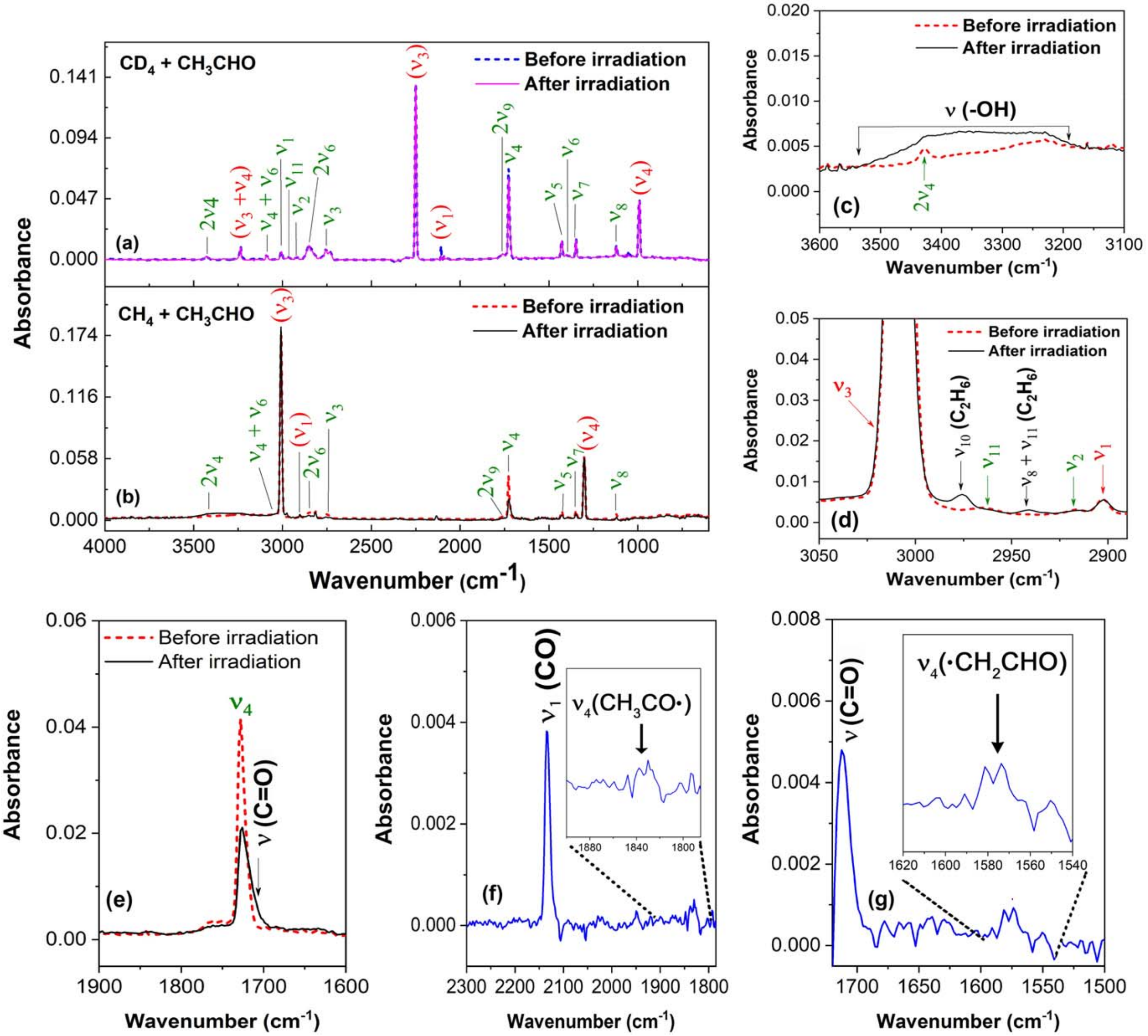

Figure 3. Infrared spectra (IR) of (a) CD_4–CH_3CHO and (b) CH_4–CH_3CHO ice mixtures before (dashed line) and after the irradiation (solid line) at a low dose (0.30 ± 0.03 eV molecule^{-1}) and a high dose (4.06 ± 0.4 eV molecule^{-1}), respectively. Assignments denoted in green and red correspond to CH_3CHO and CD_4/CH_4, respectively. (c), (d), and (e) are the magnified view of the spectral regions 3600–3100, 3050–2900, and 1900–1600 cm^{-1}, respectively, depicting new IR absorptions that appeared after the irradiation of the CH_4–CH_3CHO ice mixture at a high dose. (f) and (g) are the difference IR spectra obtained in the carbonyl stretching (C=O) region by subtracting the IR spectra measured before and after the irradiation of the CH_4–CH_3CHO ice mixture. Detailed assignments of the bands corresponding to the reactants are provided in Table 4. New infrared absorptions observed after the irradiation are tabulated in Table 5. All of the measurements were performed at 5 K.

bending) cm^{-1}. Detailed assignments of the bands corresponding to the reactants are provided in Table 4. After the irradiation at a low dose (15 nA for 5 minutes), the intensities of fundamentals linked to acetaldehyde (CH_3CHO) and d_4-methane (CD_4) decrease by $10.2\% \pm 2.0\%$ and $4.5\% \pm 0.5\%$, respectively. Furthermore, the absorption features of the predicted products were not very distinct in low-dose experiments. However, the infrared features of the products are more pronounced in the FTIR spectrum of the irradiated CH_4–CH_3CHO ice mixture (Figure 3(b)) measured after exposure to high radiation current (100 nA for 10 minutes). At a high dose, the acetaldehyde band intensities decreased by $74.4\% \pm 8.0\%$. New distinct absorption features corresponding to the products are observed in the spectral regions 3500–3200, 2972, 2938, and 2131 cm^{-1} (Table 5); magnified views of these absorption peaks are presented in Figures 3(c)–(e). The broad absorption in the region 3500–3200 cm^{-1} can be attributed to hydroxy (OH)-bearing species (Figure 3(c)), while the peaks centered at 2972 and 2938 cm^{-1} can be assigned to the CH_3 stretch and combination band of ethane (C_2H_6), respectively (Figure 3(d)). The C=O stretching vibration at 2131 cm^{-1} can be associated with carbon monoxide (CO). More importantly, three weak infrared absorptions are observed in the spectral regions 2000–1800 and 1720–1500 cm^{-1} depicted in the difference IR spectra (Figures 3(f)–(g)). The vibrational band at 1710 cm^{-1} could correspond to the carbonyl stretch of keto or (and) aldehyde functional group(s) (Figure 3(g)). The very low-intensity bands observed at 1837 cm^{-1} (Figure 3(f)) and 1573 cm^{-1} (Figure 3(g)) could be assigned to the acetyl ($CH_3\dot{C}O$) and vinoxy ($\cdot CH_2CHO$)

Table 4
Infrared Absorption Features of (CD_4 + CH_3CHO) and (CH_4 + CH_3CHO) Ice Mixtures at 5 K before Irradiation

Wavenumber (cm^{-1})		Assignment	Carrier	Reference
CD_4 + CH_3CHO	CH_4 + CH_3CHO			
3424	3427	$2\nu_4$ (CH_3CHO)	overtone	(Hollenstein & Günthard 1971; Kleimeier et al. 2020c)
3237		$\nu_3 + \nu_4$ (CD_4)	combination	(Kaiser et al. 2014)
3091	3096	$\nu_4 + \nu_6$ (CH_3CHO)	combination	(Hollenstein & Günthard 1971; Kleimeier et al. 2020c)
3010		ν_1(CH_3CHO)	CH_3 stretch	(Hollenstein & Günthard 1971; Kleimeier et al. 2020c)
	3006	ν_3(CH_4)	C–H asymm. stretch	(Kaiser et al. 2014)
2960	2969	ν_{11} (CH_3CHO)	CH_3 stretch	(Hollenstein & Günthard 1971; Kleimeier et al. 2020c)
	2904	ν_1(CH_4)	C–H symm. stretch	(Kaiser et al. 2014)
2919	2922	ν_2 (CH_3CHO)	CH_3 symm. stretch	(Hollenstein & Günthard 1971; Kleimeier et al. 2020c)
2854	2848	$2\nu_6$ (CH_3CHO)	overtone	(Hollenstein & Günthard 1971; Kleimeier et al. 2020c)
2754	2751	ν_3 (CH_3CHO)	C–H ald. stretch	(Hollenstein & Günthard 1971; Kleimeier et al. 2020c)
2250		ν_3 (CD_4)	C–D asymm. stretch	(Kaiser et al. 2014)
2109		ν_1 (CD_4)	C–D symm. stretch	(Kaiser et al. 2014)
1754	1757	$2\nu_9$ (CH_3CHO)	overtone	(Hollenstein & Günthard 1971; Kleimeier et al. 2020c)
1726	1726	ν_4 (CH_3CHO)	CO stretch	(Kaiser et al. 2014)
1430	1424	ν_5 (CH_3CHO)	CH_3 deform.	(Hollenstein & Günthard 1971; Kleimeier et al. 2020c)
1399	1399	ν_6 (CH_3CHO)	C-H bend	(Hollenstein & Günthard 1971; Kleimeier et al. 2020c)
1346	1346	ν_7 (CH_3CHO)	CH_3 deform.	(Hollenstein & Günthard 1971; Kleimeier et al. 2020c)
	1303	ν_4(CH_4)	C–H bend	(Kaiser et al. 2014)
1122	1116	ν_8 (CH_3CHO)	C–H wag.	(Hollenstein & Günthard 1971; Kleimeier et al. 2020c)
997		ν_4 (CD_4)	C–D bend	(Kaiser et al. 2014)

Table 5
New Infrared Absorption Features Observed in CH_4 and CH_3CHO Ice Mixture after Irradiation at a High Dose (100 nA for 10 Minutes)

Wavenumber (cm^{-1}) CH_4 + CH_3CHO	Assignment	Carrier	Reference
3500–3200	ν (OH)	O-H stretch	(Kleimeier et al. 2020c)
2972	ν_{10} (C_2H_6)	CH_3 stretch	(Kaiser et al. 2014)
2938	$\nu_8 + \nu_{11}$ (C_2H_6)	combination	(Kaiser et al. 2014)
2131	ν_1 (CO)	CO stretch	(Kaiser et al. 2014)
1837	ν_4 ($CH_3\dot{C}O$)	CO stretch	(Jacox 1982)
1710	ν (CO)(ketone/aldehyde)	CO stretch	(Rachid et al. 2020)
1573	ν_4 ($\cdot CH_2CHO$)	CO stretch	(Hudson & Ferrante 2019)

Note. Measurement was performed at 5 K.

radical fragments of acetaldehyde, respectively. Although the assignment of acetyl radical ($CH_3\dot{C}O$) is in good agreement with that reported by Jacox (1982) (1842 cm^{-1}) and Kleimeier et al. (2020c) (1841 cm^{-1}), the assignment of the band at 1573 cm^{-1} as the vinoxy radical ($\cdot CH_2CHO$) has to be considered tentative. This is due to the variance in the reported literature values. Jacox et al. (1982) reported the absorption of the vinoxy fragment ($\cdot CH_2CHO$) in an argon matrix at 1525 and 1541 cm^{-1}, while Hudson & Ferrante (2019) assigned the vibrational band at 1571 cm^{-1} to the carbonyl stretch of the vinoxy radical ($\cdot CH_2CHO$). It is important to note that a mixture of COMs could form after the irradiation, but they cannot be segregated via FTIR spectroscopy because their functional groups, such as the carbonyl group frequencies, often overlap. Therefore, an alternative analytical method is crucial to probe the discrete COMs formed in the processed ice mixture (Turner & Kaiser 2020). We accomplished this goal by exploiting isomer-selective PI-ReTOF-MS during the TPD phase of the irradiated ices.

3.2. PI-ReTOF-MS: Detection of Acetone, Propanal, and Propylene Oxide

The PI-ReTOF mass spectra measured as a function of temperature during the sublimation phase of processed CH_4—CH_3CHO ice mixture at a photon energy of 10.49 eV revealed a noticeable trace at a mass-to-charge (m/z) ratio of 58, which can be associated with the molecular formula C_3H_6O (Figures 4(a) and 5(a)). Further reaction products are observed at $m/z = 42$ (C_2H_2O), 72 (C_4H_8O), 86 ($C_4H_6O_2$), 88 ($C_4H_8O_2$), 89 ($C_4H_9O_2$), 101 ($C_5H_9O_2$), 117 ($C_5H_9O_3$), and 132 ($C_6H_{12}O_3$). It is important to note that no products were observed in a control (blank) experiment, where the mass spectra were recorded during the sublimation phase of the nonirradiated ice mixture while keeping all other parameters the same. Therefore, the formation of the products in the ices can be linked to the electron exposure of the ices, but not to the reactions of ions generated during the photoionization in the sublimation phase.

The TPD profile measured at $m/z = 58$ (C_3H_6O) revealed two prominent sublimation peaks centered at 210 and 240 K (Figure 5(a)). To verify the molecular formula of the product and determine which C_3H_6O isomer(s) were formed, we conducted isotopic substitution experiments with CD_4–CH_3CHO ice mixtures. The PI-ReTOF data were collected during the sublimation process at three different photon energies: 10.49, 9.80, and 9.20 eV (Figures 4(b)–(d)). At the highest photon energy, i.e., 10.49 eV, we observed a signal at $m/z = 61$, but not at 58. The TPD profile collected at $m/z = 61$ in the CD_4–CH_3CHO system (Figure 5(b)) matches the profile collected at $m/z = 58$ in the CH_4–CH_3CHO system (Figure 5(a)), thereby confirming the mass shift by 3 amu. Thus, the signal at $m/z = 61$ could be associated with the radical–radical recombination product(s), i.e., d_3-acetone (CD_3COCH_3) and/or d_3-propanal (CD_3CH_2CHO). Upon lowering the photon energy to 9.80 eV, at which d_3-propanal (CD_3CH_2CHO; IE = 9.96 ± 0.01 eV) cannot be ionized, we observed only a single sublimation peak centered at 210 K (Figure 5(c)). This suggests that the second sublimation event (230–250 K) originates from d_3-propanal (CD_3CH_2CHO). At a photon energy of 9.20 eV,

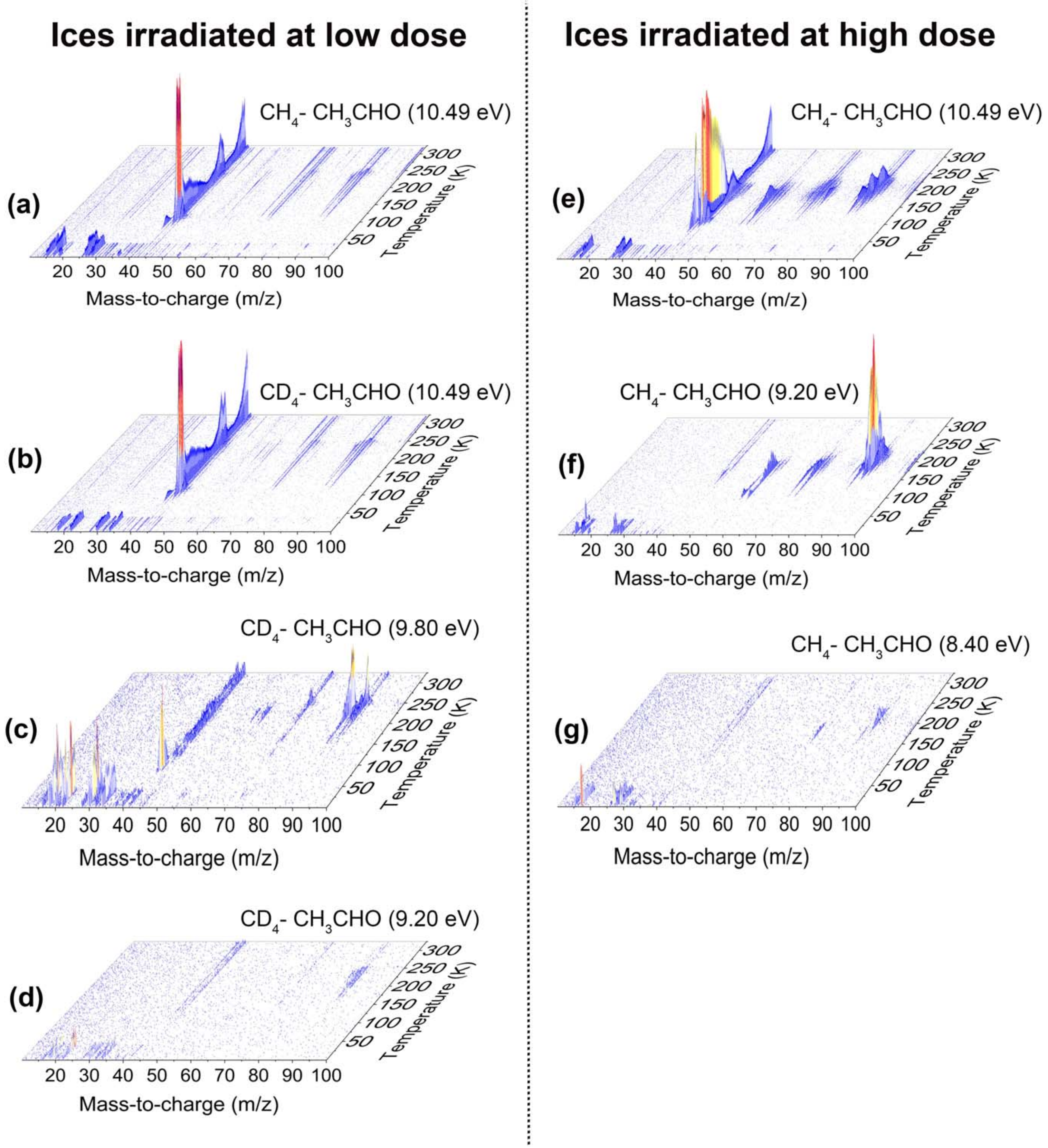

Figure 4. PI-ReTOF data collected as a function of temperature during the TPD of irradiated (low dose) (a) CH_4–CH_3CHO system at 10.49 eV, CD_4–CH_3CHO system at photon energies of (b) 10.49, (c) 9.80 and (d) 9.20 eV. (e), (f), and (g) are mass spectra measured during the TPD phase of irradiated (high dose) CH_4–CH_3CHO ice mixtures at photon energies of 10.49, 9.20, and 8.40 eV, respectively.

which is lower than the ionization energy of d_3-acetone (CD_3COCH_3; IE = 9.703 ± 0.006), no ion signal is observed (Figure 5(c)). Consequently, the sublimation peak observed at 210 K can be linked to d_3-acetone (CD_3COCH_3). Recall that the isomers formed through carbene insertion and addition could contribute to the ion signal at $m/z = 60$ in the CD_4–CH_3CHO system. The TPD trace collected at $m/z = 60$ at 10.49 eV in CD_4–CH_3CHO system revealed a single sublimation event (Figure 5(d)) that coincides with the first sublimation peak identified at $m/z = 58$ in the CH_4–CH_3CHO system; this corroborates an expected mass shift of 2 amu for the deuterated carbene addition and insertion products (Figure 5(d)). To segregate the addition product, propylene oxide-d_2 (c-CH_3CHOCD_2; IE = 10.22 ± 0.22 eV) from the insertion products, i.e., 1,1-d_2-propanal (CD_2HCH_2CHO; IE = 9.96 ± 0.01 eV), 2,2-d_2-propanal(CH_3CD_2CHO; IE = 9.96 ± 0.01 eV), and 1,1-d_2-acetone (CD_2HCOCH_3; IE = 9.700 ± 0.006 eV), we performed PI-ReTOF measurement at a photon energy of 10.10 eV, which cannot ionize

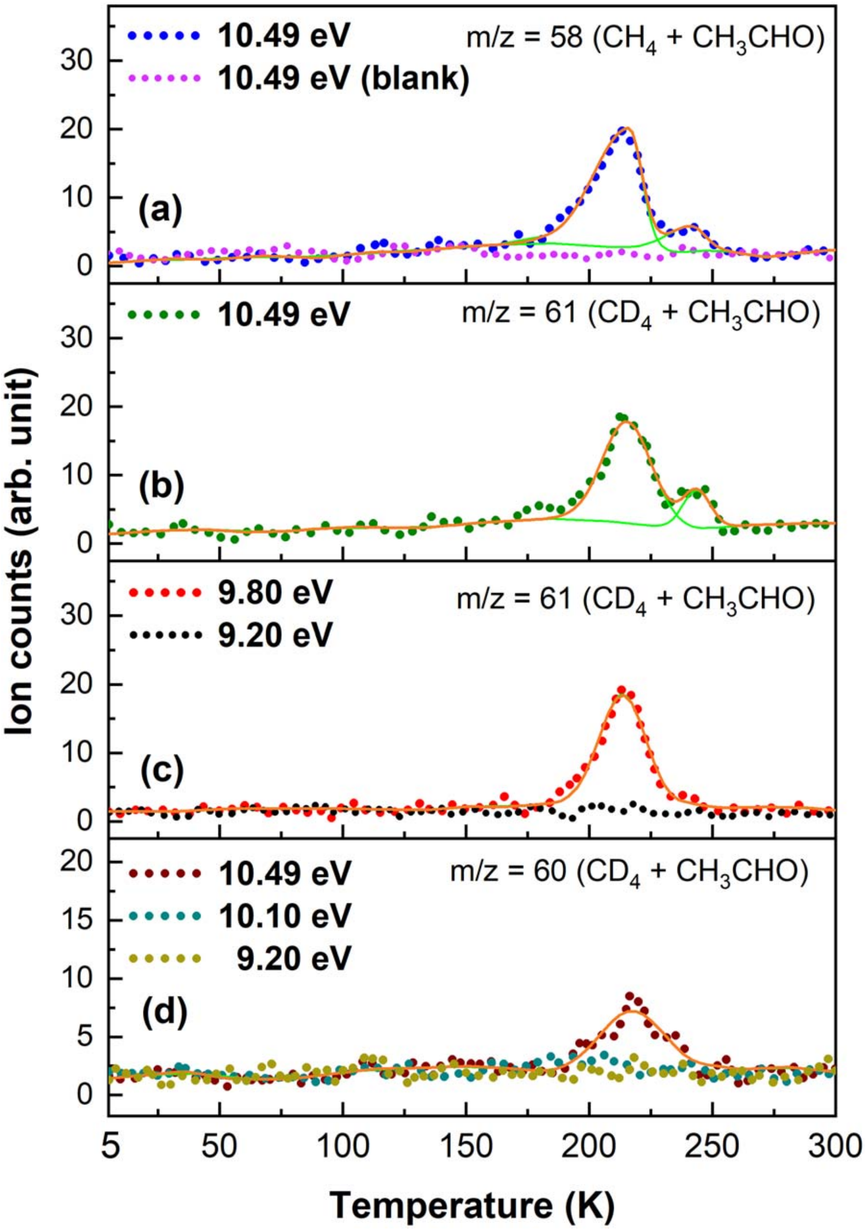

Figure 5. PI-ReTOF mass spectra measured at (a) $m/z = 58$ during the sublimation phase of irradiated (at low dose) and nonirradiated (blank) CH_4–CH_3CHO system using a photon energy of 10.49 eV. Sublimation profiles were recorded in the mass spectra of irradiated (at low dose) CD_4–CH_3CHO ice mixtures at $m/z = 61$ using photon energies of (b) 10.49, (c) 9.80, and 9.20 eV as well as at $m/z = 60$ employing photon energies of (d) 10.49, 10.10 and 9.20 eV. Spectra were deconvoluted using the bi-Gaussian peak-fitting function to identify the individual peak positions. The solid green and orange lines indicate the individual peak fits and the total fit, respectively.

the addition product, only the insertion products. The TPD trace collected at 10.10 eV revealed no signal at $m/z = 60$ (Figure 5(d)), confirming the presence of d_2-propylene oxide (c-CH_3CHOCD_2) and the absence of insertion products in the reaction mixture. The noise level in the PI-ReTOF measurements is displayed in Figure A1 of the Appendix for comparison.

Other possible C_3H_6O isomers such as methyl vinyl ether (CH_2CHOCH_3), cyclopropanol (c-CH_2CH_2CHOH), 1-propenol ($CH_3CHCHOH$), prop-1-en-2-ol ($CH_3C(OH)CH_2$), and trimethylene oxide (oxetane; c-$CH_2CH_2CH_2O$) can be disregarded based on the following experimental observations. The IEs of methyl vinyl ether (CH_2CHOCH_3; $IE = 8.95 \pm 0.01$ eV), 1-propenol ($CH_3CHCHOH$; $IE = 8.64 \pm 0.02$ eV), prop-1-en-2-ol ($CH_3C(OH)CH_2$; $IE = 8.60 \pm 0.10$ eV), and cyclopropanol (c-CH_2CH_2CHOH; $IE = 9.10$ eV) are lower than 9.20 eV. In the CD_4 + CH_3CHO ice mixture, if doubly and triply deuterated methyl vinyl ether, 1-propenol, prop-1-en-2-ol, and cyclopropanol would form in the reaction mixture, then we should observe their mass signals at $m/z = 61$ and 60 upon photoionization at 9.20 eV. In PI-ReTOF measurement at a photon energy of 9.20 eV, we did not observe any signals at $m/z = 60$ and 61 (Figures 5(c) and (d)); this suggests that doubly and triply deuterated methyl vinyl ether, 1-propenol, prop-1-en-2-ol, and cyclopropanol are not formed in the reaction mixture at the given experimental conditions. In CD_4 + CH_3CHO ice mixture, the d_2-trimethylene oxide (c-$CD_2CH_2CH_2O$; $IE = 9.65 \pm 0.01$ eV) is most likely to form via a two-step process. The first step would involve an electrophilic attack of d_2-carbene on the oxygen atom of acetaldehyde (CH_3CHO), followed by a concerted ring formation and hydrogen migration reaction. If

d_2-trimethylene oxide (c-$CD_2CH_2CH_2O$) is formed in the reaction mixture, its mass signal should appear at $m/z = 60$ at a photon energy of 10.10 eV. In the PI-ReTOF measurement conducted at a photon energy of 10.10 eV, we did not observe any signal at $m/z = 60$ (Figure 5(d)), implying that d_2-trimethylene oxide is not formed under the given experimental conditions.

Butane ($CH_3CH_2CH_2CH_3$) and isobutane ($HC(CH_3)_3$) are yet other molecules that have the same molecular mass as C_3H_6O isomers; however, their ionization energies of 10.53 ± 0.02 eV and 10.68 ± 0.11 eV, respectively, indicate that these molecules cannot be ionized at a photon energy of 10.49 eV. Therefore, the mass signal observed at $m/z = 61$ at a photon energy of 10.49 eV (Figure 5(b)) cannot be associated with partially deuterated butane and isobutane. It is also important to note here that among methyl vinyl ether (CH_2CHOCH_3), cyclopropanol (c-CH_2CH_2CHOH), 1-propenol ($CH_3CHCHOH$), and prop-1-en-2-ol ($CH_3C(OH)CH_2$), the latter two isomers can directly originate from propanal (CH_3CH_2CHO) and acetone (CH_3COCH_3) via keto–enol isomerization. Synthesis of methyl vinyl ether (CH_2CHOCH_3), cyclopropanol (c-CH_2CH_2CHOH), and oxetane (c-$CH_2CH_2CH_2O$) in CH_4 + CH_3CHO ice mixture would likely involve suprathermal oxygen atoms (O) or alkoxy (OR) radical reactive intermediate. Radiolysis studies of solid acetaldehyde suggest that acetyl and vinoxy radical species are primarily produced. (Belevskii et al. 1985; Feldman et al. 2001; Swiderek et al. 2007) and no evidence of alkoxy (OR) or oxygen atom has been reported. Therefore, the reaction pathways involving only acetyl ($CH_3\dot{C}O$) and vinoxy ($\cdot CH_2CHO$) radicals of acetaldehyde are investigated here.

3.3. PI-ReTOF-MS: Detection of Enols

Having established the detection of acetone (CH_3COCH_3), propanal (CH_3CH_2CHO), and propylene oxide (c-CH_3CHOCH_2) as "first generation" products, we are exploring now the possibility of the enolization of the ketone and aldehyde at higher doses. For this purpose, the CH_4-CH_3CHO ice mixtures were exposed to a higher radiation dose. It is important to note here that exposing the CD_4-CH_3CHO system to a high dose would result in isotopic scrambling, which will complicate the analysis; therefore, high-dose experiments are not performed with CD_4–CH_3CHO ice mixtures. PI-ReTOF data collected during the sublimation phase of processed CH_4–CH_3CHO ices (high dose) at photon energies of 10.49, 9.20, and 8.40 eV are depicted in Figures 4(e)–(g) and 6. Intriguingly, the TPD trace collected at $m/z = 58$ at a photon energy of 10.49 eV revealed a broad sublimation event ranging from 100 to 225 K with a central peak at 175 K and three shoulders at 110, 132, and 207 K (Figure 6(a)). A significant change in the TPD profile of $m/z = 58$ between high- and low-dose experiments suggests a drastic chemical change in the ices. This observation is also well supported by FTIR spectroscopy, which suggests that more than 50% of acetaldehyde molecules dissociate. In detail, a deconvolution of the TPD profile measured at $m/z = 58$ employing a bi-Gaussian peak-fitting function revealed five peak components, centered at 110, 132, 156, 175, and 207 K and are labeled as I, II, III, IV, and V respectively. To identify the sublimation peaks corresponding to enols, we have performed PI-ReTOF measurements at 9.20 eV; at this photon energy, only enol isomers 1-propenol and prop-1-en-2-ol can be ionized (Figure 1). The TPD profile collected at 9.20 eV showed the absence of shoulder peaks II and V (Figure 6(b)). Further, no signal is detected at photon energies (8.20 eV) below the IEs of the enols. Based on these results, we conclude that peaks I, III, and IV belong to enols. Since the range of the IEs of 1-propenol (8.53–8.66 eV) and prop-1-en-2-ol (8.50-8.86 eV) overlap, they cannot be distinguished based on their IEs in TPD PI-ReTOF experiments. Note that peaks II and V observed at 10.49 eV could be associated with first-generation products. Separate calibration experiments performed for acetone and propanal by codepositing 0.7% acetone and 1% propanal in CH_4–CO ice mixture followed by PI-ReTOF measurements also show that the TPD traces of acetone and propanal are overlapped with peaks centered at 125 K and 120 K, respectively (Figure A2). Following the results of low-dose experiments and calibration experiments, we can imply that in 10.49 eV data, the ion counts in peak region II are due to contribution from acetone, propanal, and propylene oxide.

It is important to recall here that in low-dose experiments, the peak sublimation temperatures of acetone (210 K) and propanal (240 K) are higher than the ones measured in high-dose experiments and calibration experiments. Previous studies performed with pure acetaldehyde (CH_3CHO) ices revealed that acetaldehyde polymerizes upon exposure to radiations to form polymer-like chains either by radical reactions with the neighboring molecules (Chaechaty & Marx 1961) or by ionic reactions, as suggested by A. Charlesby (1965). At a low dose, polar products such as acetone and propanal could be trapped inside the polymer matrix of acetaldehyde; as a result, their sublimation event initiates at a higher temperature (210 K and 240 K). Contrary to acetone (CH_3COCH_3), propanal (CH_3CH_2CHO) is a better hydrogen bond donor as well as acceptor; the later molecule can form stronger hydrogen bonds with the polymer-like matrix of the acetaldehyde; this could cause sublimation of propanal at a higher temperature than acetone (CH_3COCH_3). At a high dose or prolonged radiation exposure, the polymer-like chains of acetaldehyde may be decomposed into small-molecular-weight products, thereby reducing the matrix-cage effects. These assertions are also supported by the fact that in low-dose experiments, the sublimation profile of acetaldehyde (CH_3CHO) measured at $m/z = 44$ ranges from 90 to 300 K with three major peaks centered at 113, 144, and 242 K, implying that acetaldehyde molecules are coupled in a polymer-like motif, which sublimes over a broad temperature range (Figure A3(a)). On the other hand, at a high dose, only two major sublimation events peaking at 113 and 145 K are observed in the TPD profile of acetaldehyde; the majority of acetaldehyde molecules sublime in the temperature range of 90–200 K (Figure A3(b)).

The origin of peak V at $m/z = 58$ could be ascertained from fragments of higher molecular weight product observed at $m/z = 102$ ($C_5H_{10}O_2$). The TPD profile measured at $m/z = 102$ ($C_5H_{10}O_2$) at 10.49 eV is in good agreement with the peak V observed at $m/z = 58$ (Figure A4). Although our PI-ReTOF-MS studies could not directly discriminate the nature of the enol isomers (1-propenol and/or prop-1-en-2-ol), the sublimation profile of 1-propenol measured by Abplanalp et al. (Abplanalp et al. 2016) can assist in distinguishing the enol species observed in the present high-dose experiment. Abplanalp et al. determined the peak sublimation temperature of 1-propenol to about 165 K, which is in excellent agreement with the sublimation peak region IV (Figure 6(b)) centered at 170 K. Hence, among enols peaks I, III, and IV, observed at $m/z = 58$ at a photon energy of 9.20 eV (Figure 6(b)), at least peak IV can be assigned to 1-propenol, while peak regions I and III can be ascertained to prop-1-en-2-ol isomers.

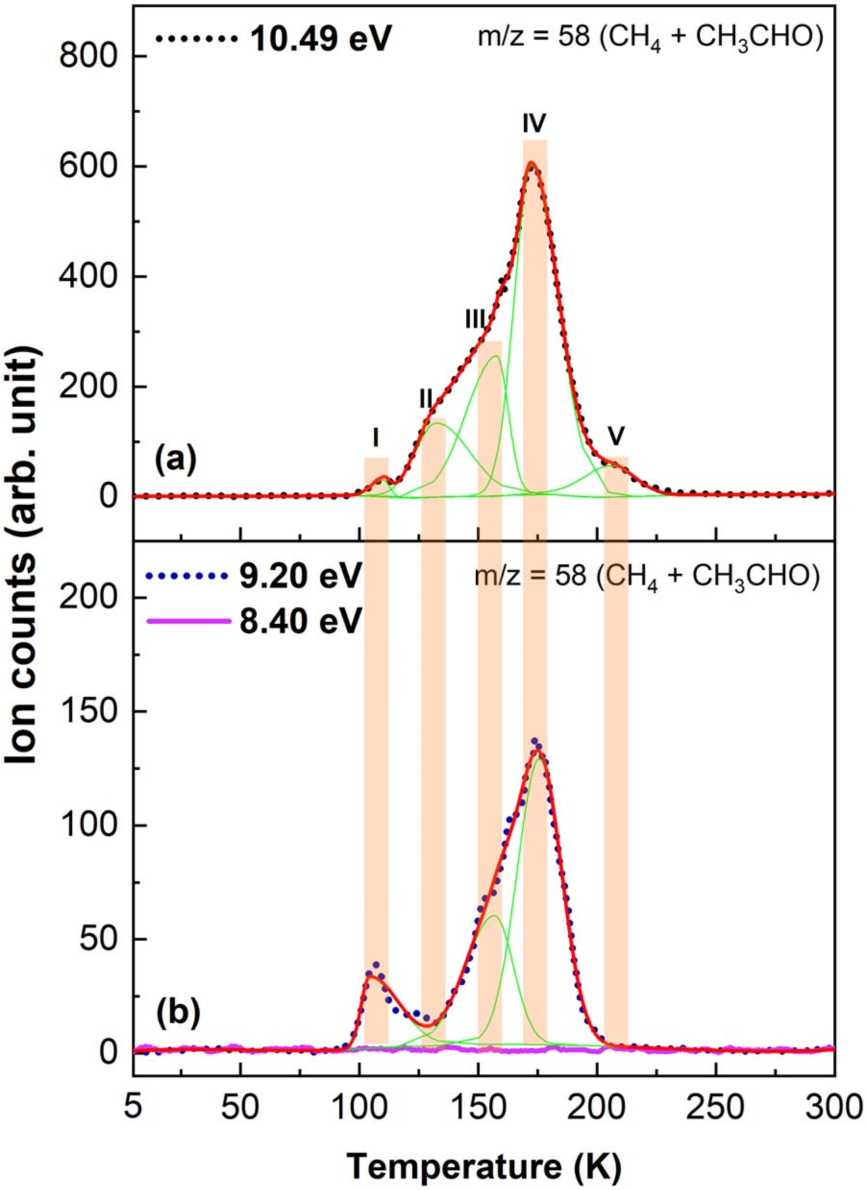

Figure 6. PI-ReTOF-MS data measured at $m/z = 58$ during the temperature-programmed desorption of irradiated (at high dose) CH_4–CH_3CHO system at photon energies of (a) 10.49, (b) 9.20, and 8.40 eV. Spectra measured at 10.49 and 9.20 eV are deconvoluted using the bi-Gaussian peak-fitting function to identify the individual peak positions. The solid green and red lines indicate individual peak fits and total fit, respectively.

3.4. Isomer Branching Ratios

The determination of the branching ratios (BRs) of the experimentally observed isomers would help understand the conditions during their formation. The BRs of species A over B can be calculated by utilizing their photoionization cross sections (σ) and the integrated PI-ReTOF ion counts. Suppose the isomers are formed via the thermal equilibrium process during the sublimation phase. In that case, this pathway is connected with the equilibrium constant K, which can be defined as $[A]/[B] = \exp(-\Delta G/RT)$, where $[A]/[B]$ is the concentration ratio of isomers A and B at temperature T, with R being the gas constant and ΔG is the difference in standard Gibbs free energies of the isomers. Upon thermodynamic equilibrium, the propanal:acetone abundance ratio of 2.5×10^{307} at 5 K to 1.9×10^7 at 210 K and propanal:propylene oxide abundance ratio of 2.8×10^{774} at 5 K to 2.7×10^{18} at 210 K are expected. A comparison of these predicted ratios with the experimentally derived BRs of 4.82 ± 0.05:1 (acetone:propanal) and of 2.86 ± 0.13:1 (propylene oxide:propanal) (Table 6) indicates an overproduction of acetone and propylene oxide in our experiment. These results signify that products are not formed under thermal equilibrium conditions, but rather through nonequilibrium processes within the ice at ultralow temperatures. The photoionization cross sections adopted in these calculations were $11.49 \pm 0.10 \times 10^{-18}$ cm^2 for acetone, $9.51 \pm 0.16 \times 10^{-18}$ cm^2 for propanal, and $8.20 \pm 0.50 \times 10^{-18}$ cm^2 for propylene oxide at 10.49 eV (Wang et al. 2008; Zhou et al. 2009; Yang & Combustion Team 2017). Finally, the absolute yields of acetone, propylene oxide, and propanal can be calculated (Bergantini et al. 2017), accounting for the photoionization cross section of acetaldehyde ($7.4 \pm 1.9 \times 10^{-18}$ cm^2) (Cool et al. 2003) versus acetone, propylene oxide, and propanal at 10.49 eV. This results in production yields of acetone, propylene oxide, and propanal to be $5.2 \pm 1.8 \times 10^{14}$, $1.6 \pm 0.5 \times 10^{14}$, $6.6 \pm 2.0 \times 10^{13}$ molecules, respectively, for the low-dose study. This translates into

Table 6

Photoionization Cross Sections (σ) of Acetone, Propanal, and Propylene Oxide at 10.49 eV and the Relative Branching Ratio of Acetone to Propylene Oxide and Propanal Observed in the Present Study

Molecule	Photoionization Cross Section (σ, cm^2)	Branching Ratio
		acetone:propylene oxide:propanal
acetone	$11.49 \pm 0.10 \times 10^{-18}$ (Zhou et al. 2009)	(4.82 ± 0.05):(2.86 ± 0.13):1
propanal	$9.51 \pm 0.16 \times 10^{-18}$ (Wang et al. 2008)	
propylene oxide	$8.20 \pm 0.50 \times 10^{-18}$ (Yang & Combustion Team 2017)	

rates of acetone, propylene oxide, and propanal of $1.8 \pm 0.4 \times 10^{-3}$, $5.4 \pm 2.0 \times 10^{-4}$, $2.2 \pm 0.8 \times 10^{-4}$ $molecules eV^{-1}$, respectively.

3.5. Reaction Mechanisms

The detailed mechanistical studies performed with the CD_4–CH_3CHO system reveal that the unimolecular dissociation of acetaldehyde (CH_3CHO) to the acetyl radical ($CH_3\dot{C}O$) and a hydrogen atom is the dominant pathway (reaction (1)); this process is endoergic by 377 $kJ\ mol^{-1}$ with the energy supplied by the impinging electrons. The d_3-methyl radical ($\cdot CD_3$) formed from d_4-methane (CD_4) via C–D bond rupture (reaction (2)) reacts with the acetyl radical barrierlessly in an exoergic reaction to form d_3-acetone (reaction (3)) provided both the reactants have a favorable recombination geometry in the ices. Decomposition of acetaldehyde to vinoxy radical ($\cdot CH_2CHO$) and a hydrogen atom through C–H bond dissociation is also feasible at a low dose (reaction (4)); this endoergic process (411 $kJ\ mol^{-1}$) was not detected in a previous study investigating the formation of 2,3-butanedione in acetaldehyde-rich ices (Kleimeier et al. 2020c). Identification of d_3-propanal (CD_3CH_2CHO) supports the possibility of radical–radical recombination of d_3-methyl ($\cdot CD_3$) and vinoxy radicals ($\cdot CH_2CHO$) in our experiments; this reaction is exoergic by 344 $kJ\ mol^{-1}$ (reaction (5)). The appearance of vinoxy radicals ($\cdot CH_2CHO$) in the processed CH_4–CH_3CHO ice mixture is also supported by FTIR spectroscopy (Section 3.1):

$$CH_3CHO \rightarrow CH_3\dot{C}O + H \quad \Delta_r G = 377\ kJ\ mol^{-1} \tag{1}$$

$$CD_4 \rightarrow \cdot CD_3 + D \quad \Delta_r G = 429\ kJ\ mol^{-1} \tag{2}$$

$$CH_3\dot{C}O + \cdot CD_3 \rightarrow CH_3COCD_3 \quad \Delta_r G = -390\ kJ\ mol^{-1} \tag{3}$$

$$CH_3CHO \rightarrow \cdot CH_2CHO + H \quad \Delta_r G = 411\ kJ\ mol^{-1} \tag{4}$$

$$\cdot CH_2CHO + \cdot CD_3 \rightarrow CD_3CH_2CHO\ \Delta_r G = -344\ kJ\ mol^{-1} \tag{5}$$

$$CD_4 \rightarrow :CD_2(X^3B_1) + 2D\ \Delta_r G = 897\ kJ\ mol^{-1} \tag{6}$$

$$CD_4 \rightarrow :CD_2(a^1A_1) + 2D \quad \Delta_r G = 495\ kJ\ mol^{-1} \tag{7}$$

$$CH_3CHO +:\ CD_2(X^3B_1) \rightarrow c - CH_3CHOCD_2 \quad \Delta_r G = -330\ kJ\ mol^{-1} \tag{8}$$

$$CH_3CHO +:\ CD_2(a^1A_1) \rightarrow c - CH_3CHOCD_2 \quad \Delta_r G = -368\ kJ\ mol^{-1} \tag{9}$$

The deuterated methane (CD_4) could also generate triplet/singlet d_2-methylene ($:CD_2$) (reactions (6)/(7)). The triplet/singlet carbene could add to the C=O bond of acetaldehyde (CH_3CHO) if the reactants have a favorable recombination geometry in the ices to form d_2-propylene oxide (c-CH_3CHOCD_2) (reactions (8) and (9)) with the reaction of singlet carbene being barrierless. The hydrogen/deuterium atoms produced in reactions (1), (2), and (4) may react back with the parent radical species to recycle the parent molecule (Kaiser et al. 1997). The hydrogen/deuterium atoms could also add to the C=O bond of acetaldehyde to form H/D-ethanol if they have sufficient kinetic energy to overcome the barrier to reaction. A recent study performed by Krim et al. (2018) suggests that the simplest aldehyde, formaldehyde, can be easily reduced to methanol via the addition of hydrogen to the C=O bond; however, higher aldehydes such as propanal and methyl formate do not form alcohol via hydrogen-addition reaction due to high energy barrier. On the other hand, the hydrogen atom bombardment of acetaldehyde ices was found to produce ethanol along with methane, formaldehyde, and methanol (Bisschop et al. 2007). In our study, reactions such as hydrogenation of acetaldehyde, if they occur, do not affect the formation of methyl acetyl and vinoxy radicals that leads to the generation of acetone and propanal.

Overall, the BR of the products suggests that the radical–radical recombination of acetyl and methyl radicals is a favorable and dominant reaction pathway to acetone in the methane–acetaldehyde ice mixture, reinforcing that acetaldehyde predominantly decomposes to the acetyl radical ($CH_3\dot{C}O$) and only to a minor amount to the vinoxy radical ($\cdot CH_2CHO$) under our experimental condition. Note that the addition pathway of singlet d_2-methylene leading to d_2-propylene oxide (c-CH_3CHOCD_2) represents a strong analogy to the addition of singlet carbene to the N=O double bond in nitrosyl hydride (HNO) (Singh et al. 2020a) and nitrous acid (HONO) (Singh et al. 2020b), forming the cyclic oxaziridine (c-H_2CONH) and *N*-hydroxyoxaziridine (c-$H_2CON(OH)$) molecules. The corresponding enols (1-propenol and/or prop-1-en-2-ol) can be formed via hydrogen shift from the methyl group to the oxygen atom in propanal (CH_3CH_2CHO) and acetone (CH_3COCH_3), respectively. These processes are similar to the enolization of acetaldehyde (CH_3CHO) to vinyl alcohol (C_2H_3OH), and glycolaldehyde ($HOCH_2CHO$) to 1,2-ethenediol (HOCHCHOH) (Abplanalp et al. 2016; Kleimeier et al. 2021b; Kleimeier & Kaiser 2021) studied previously in our laboratory.

4. Astrophysical Implications and Conclusions

In the present work, we conducted laboratory simulation experiments in astrophysically relevant ices to unravel the chemical processes that enable the formation of distinct C_3H_6O isomers in processed acetaldehyde-methane ices: acetone (CH_3COCH_3), propanal (CH_3CH_2CHO), propylene oxide (c-CH_3CHOCH_2), 1-propenol ($CH_3CHCHOH$), and tentatively prop-1-en-2-ol ($CH_3C(OH)CH_2$) isomers. Methane ;(CH_4) has been detected in the solid phase on icy interstellar grains at fractions of a few percent (Lacy et al. 1991). Although

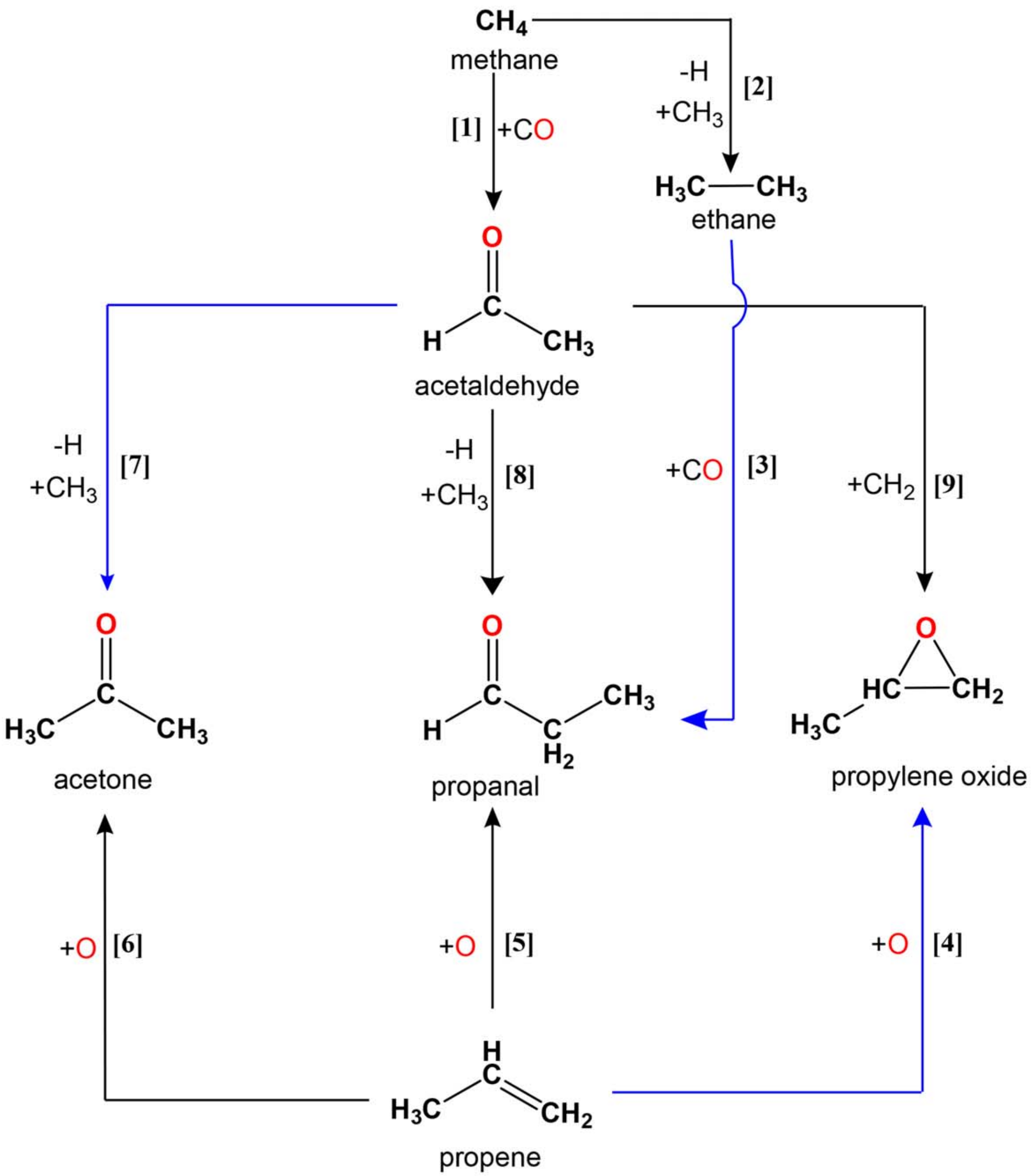

Figure 7. Reaction scheme depicting the reaction channels leading to acetaldehyde, acetone, propanal, and propylene oxide in interstellar ices upon exposure to ionizing radiations. The blue-colored arrows indicate the dominating pathways observed in previous laboratory simulation experiments in our group; see text for a detailed discussion.

acetaldehyde (CH_3CHO) has been observed only in the gas phase of the ISM, previous laboratory simulation experiments in conjunction with astrochemical modeling reveal that acetaldehyde could form in the interstellar ices at temperatures as low as 10 K via processing of methane with oxygen-bearing species such as carbon monoxide (CO) upon exposure to galactic cosmic-ray proxies (GCRs) (reaction 1; Figure 7) (Abplanalp et al. 2016). The models that included the cosmic-ray-driven nonequilibrium ice chemistry provided an excellent agreement between the theoretically predicted ($2.75 \pm 0.06 \times 10^{14}$ molecules cm^{-2}) and observed ($2.2 \pm 1.1 \times 10^{14}$ molecules cm^{-2}) (Nummelin et al. 1998) column density of acetaldehyde toward SgrB2(N) at the age of 10^6 yr. (Abplanalp et al. 2016)

Methane could also dissociate into a methyl radical and a hydrogen atom upon exposure to GCRs. Previous laboratory experiments with solid methane confirmed the detection of methyl radicals and hydrogen atoms after exposure to ionizing radiations (Smaller & Matheson 1958; Wall et al. 1959; Brown et al. 1962). Radical–radical recombination reactions between methyl radicals in the ices could lead to the synthesis of ethane (C_2H_6) (reaction 2; Figure 7) as well as higher-order hydrocarbons (Abplanalp et al. 2018). Intriguingly, ethane (C_2H_6) could also react with carbon monoxide (CO) to form propanal (CH_3CH_2CHO) (reaction 3; Figure 7) and 1-propenol via nonequilibrium pathways inside the icy interstellar grains during the radiation exposure; however, the synthesis of acetone (CH_3COCH_3) or propylene oxide was not observed in ethane–carbon monoxide ices (Abplanalp et al. 2016). Propanal (CH_3CH_2CHO) was also detected in processed the H_2O + CH_3OH + NH_3 interstellar ice analog, along with acetaldehyde

(CH_3CHO), possibly lactaldehyde ($CH_3CH(OH)CHO$), glycolaldehyde ($CH_2(OH)CHO$), and glyceraldehyde ($CH_2(OH)CH(OH)CHO$) but no evidence of acetone was documented (de Marcellus et al. 2015). Qasim et al. reported the synthesis of possibly propanal in a nonenergetically processed $C_2H_2 + CO + H$ ice mixture via radical–radical recombination of $H\dot{C}O$ and $H_3C\dot{C}H_2$ radicals (Qasim et al. 2019).

Laboratory astrophysics simulation experiments coupled with astrochemical modeling revealed that the reaction of suprathermal oxygen atoms ($O(^3P/^1D)$) with propene (CH_3CHCH_2) eventually generates predominantly propylene oxide (c-CH_3CHOCH_2) and to a smaller amount propanal (CH_3CH_2CHO) and acetone (CH_3COCH_3) following nonequilibrium reaction processes (reactions 4–6; Figure 7) (Bergantini et al. 2018a). Interestingly, propylene oxide represents the dominant product; the experimental BRs of propylene oxide:acetone:propanal were derived to be (92 ± 4): (23 ± 7): 1. Hudson et al. have also investigated the formation of propylene oxide, propanal, and acetone in irradiated $CO_2 + C_3H_6$ ice mixture. However, IR features of only propylene oxide and propanal were assigned firmly (Hudson et al. 2017); the $C{=}O$ vibrational feature that could correspond to acetone was very weak to allocate affirmatively. Molecular collision of ground-state atomic oxygen ($O(^3P)$) with propene (C_3H_6) thin films also yields propylene oxide, propanal, and acetone, but only the first two molecular species were formed in higher concentration (Brann et al. 2020). The suprathermal oxygen atoms required in reactions (4), (5), and (6) (Figure 7) could originate from oxygen-containing molecules such as the CO_2, CO, and O_2 present within the interstellar ices through interaction with cosmic rays (Maity et al. 2014b), while propene (CH_3CHCH_2) could form in the interstellar ice via the reaction of ethane (C_2H_6) with methylidyne (CH) (Abplanalp et al. 2018, 2019). Astrochemical modeling suggests that the observed fractional abundances of propylene oxide (c-CH_3CHOCH_2) toward Sgr B2(N) (McGuire et al. 2016) are in excellent agreement with theoretically predicted data determined by including the cosmic-ray-triggered ice chemistry, at an age close to 10^6 yr (Bergantini et al. 2018a).

Overall, COMs such as C_3H_6O isomers acetone (CH_3COCH_3), propanal (CH_3CH_2CHO), propylene oxide (c-CH_3CHOCH_2), 1-propenol ($CH_3CHCHOH$), and prop-1-en-2-ol ($CH_3C(OH)CH_2$) can be formed via multiple pathways in interstellar ices as compiled in Figure 7. The outcome of the reaction and hence the branching ratios strongly depend on the nature of the reactants within the ices. Careful quantitative experimental studies such as the present project are required to shed light on these underlying formation pathways based on solid laboratory data such as formation rates. These isomers and reactant-specific production rates can then be incorporated into the next generation of astrophysical models in an attempt to replicate astronomical observations of complex organics such as those structural isomers of the C_3H_6O system as presented here.

We acknowledge the W. M. Keck Foundation for financing the experimental setup. Financial support from the US National Science Foundation (NSF) Division of Astronomical Sciences (AST) 2103269 awarded to the University of Hawaii (R.I.K) is greatly acknowledged. N.F.K. acknowledges funding from the Deutsche Forschungsgemeinschaft (DFG, German Research Foundation) for a postdoctoral fellowship (KL 3342/1-1). A.K.E. thanks Fonds der Chemischen Industrie (Liebig Fellowship) and the Deutsche Forschungsgemeinschaft (DFG, German Research Foundation) under Germany's Excellence Strategy – EXC-2033 – 390677874 - RESOLV for funding.

Appendix

Figure A1 shows the noise level in the PI-ReTOF measurements. The TPD profiles of acetone and propanal measured in the calibration experiment are depicted in Figure A2. The sublimation profiles of acetaldehyde measured during the TPD phase of $CH_4 + CH_3CHO$ ice mixture irradiated at low dose and high dose are compared in Figure A3. Figure A4 compares the TPD profiles of the products observed at $m/z = 102$ and $m/z = 58$ in the PI-ReTOF measurement of irradiated (high dose) $CH_4 + CH_3CHO$ ice mixture.

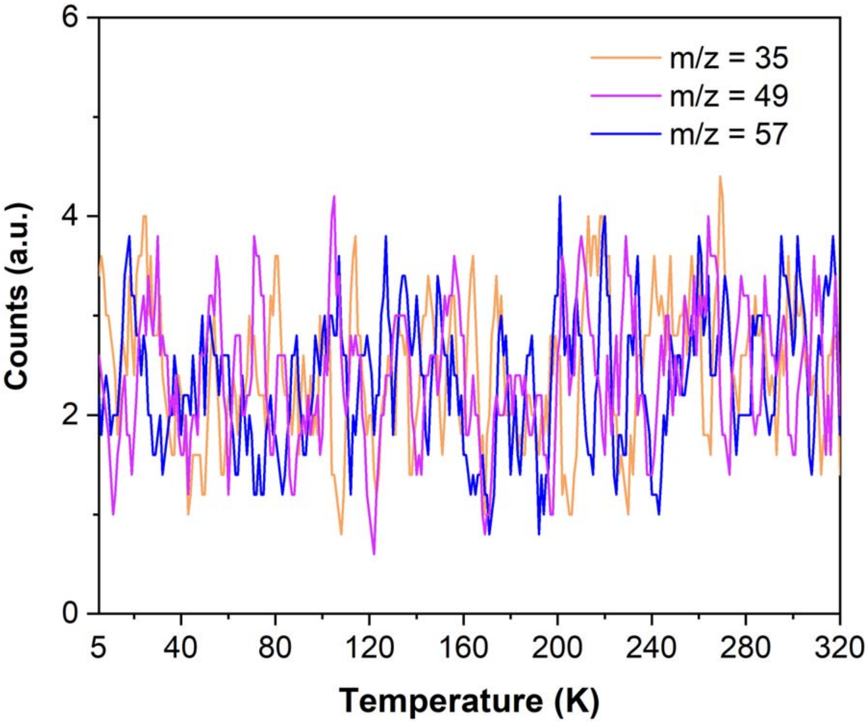

Figure A1. PI-ReTOF mass spectra measured at a photon energy of 10.10 eV at *m/z* = 35, 49, and 57 during the TPD phase of the $CD_4 + CH_3CHO$ ice mixture. These data are provided to show the noise level in the PI-ReTOF measurements.

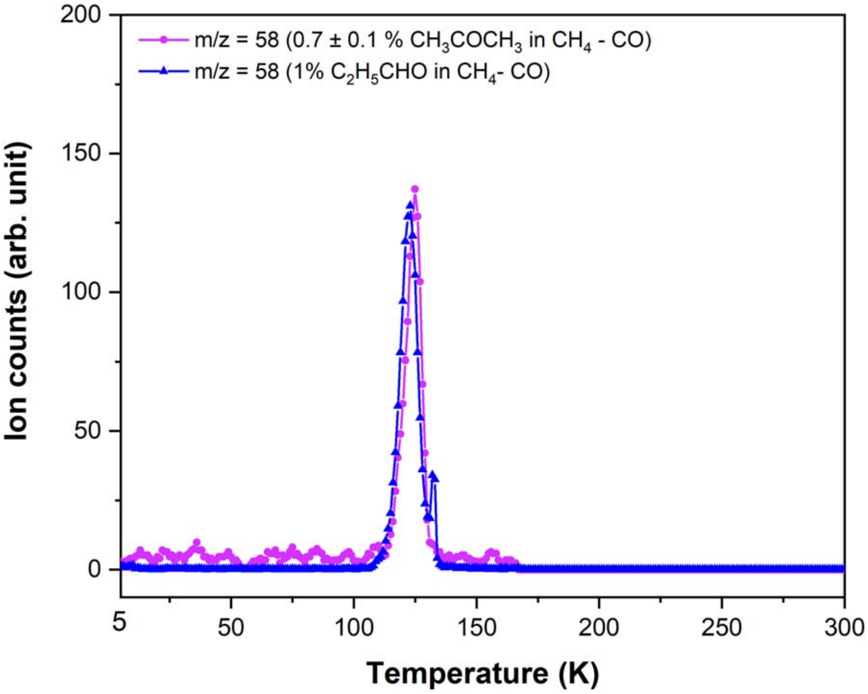

Figure A2. TPD profiles measured at *m/z* = 58 during the sublimation phase of the nonirradiated ice mixtures containing 0.7% acetone in CH_4–CO, and 1% propanal in CH_4-CO at a photon energy of 10.49 eV.

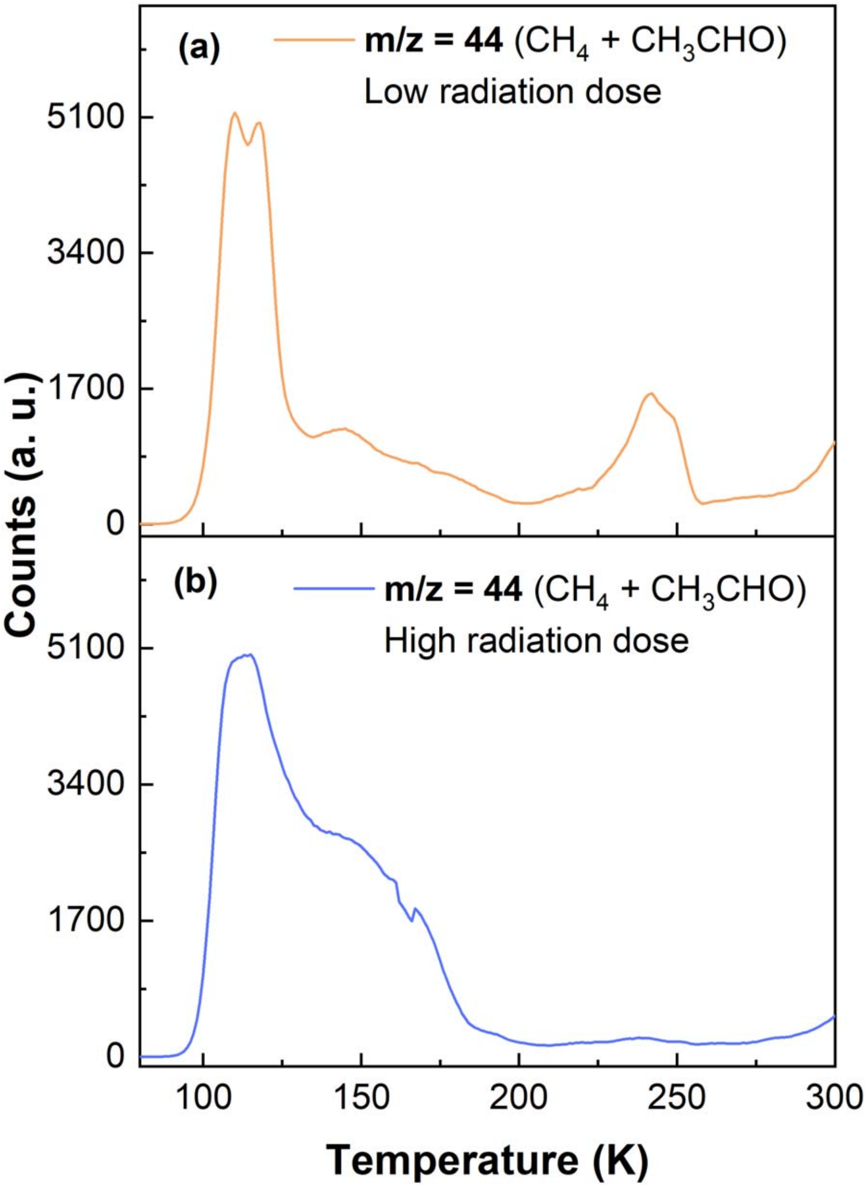

Figure A3. PI-ReTOF mass spectra measured at *m/z* = 44 at a photon energy of 10.49 eV during the TPD phase of CH_4+CH_3CHO ice mixture irradiated at (a) low dose and (b) high dose.

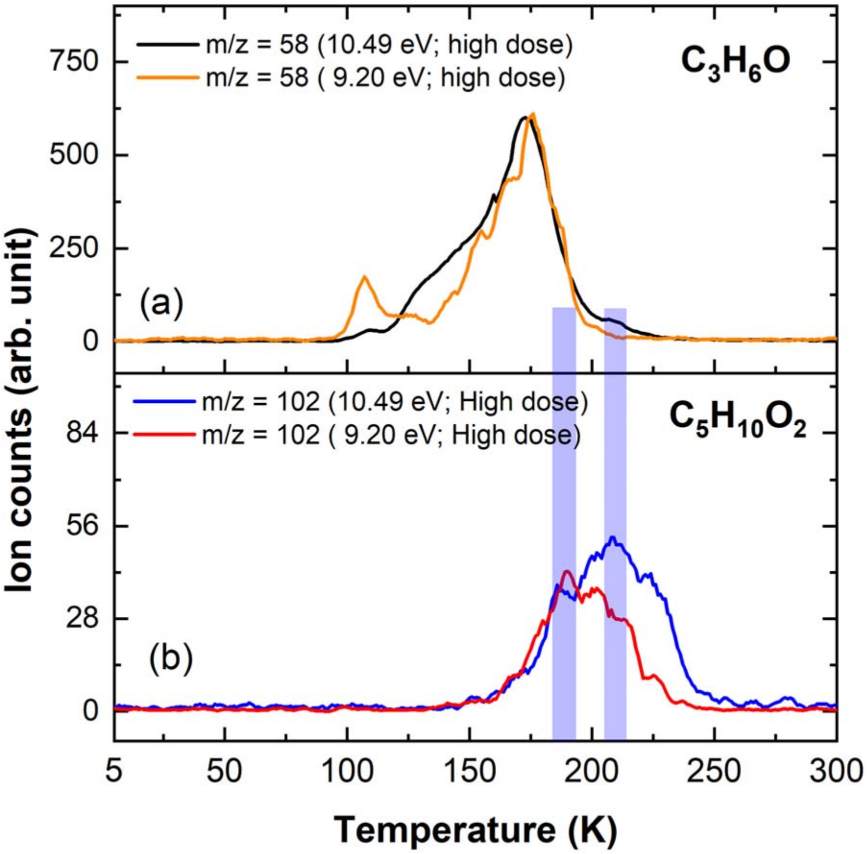

Figure A4. TPD profiles measured at (a) $m/z = 58$ and (b) $m/z = 102$ in irradiated CH_4–CH_3CHO system at photon energies of 10.49 and 9.20 eV.

ORCID iDs

André K. Eckhardt https://orcid.org/0000-0003-1029-9272
Ralf I. Kaiser https://orcid.org/0000-0002-7233-7206

References

Abplanalp, M. J., Góbi, S., & Kaiser, R. I. 2019, PCCP, 21, 5378
Abplanalp, M. J., Gozem, S., Krylov, A. I., et al. 2016, PNAS, 113, 7727
Abplanalp, M. J., Jones, B. M., & Kaiser, R. I. 2018, PCCP, 20, 5435
Abplanalp, M. J., & Kaiser, R. I. 2019, PCCP, 21, 16949
Andrade, D. P. P., de Barros, A. L. F., Ding, J., et al. 2014, MNRAS, 444, 3792
Arumainayagam, C. R., Garrod, R. T., Boyer, M. C., et al. 2019, ChSRv, 48, 2293
Becke, A. D. 1988, PhRvA, 38, 3098
Belevskii, V. N., Belopushkin, S. I., & Feldman, V. I. 1985, JRNC, 96, 137
Bennett, C. J., Brotton, S. J., Jones, B. M., et al. 2013, AnaCh, 85, 5659
Bennett, C. J., Chen, S. H., Sun, B. J., Chang, A. H. H., & Kaiser, R. I. 2007, ApJ, 660, 1588
Bennett, C. J., Jamieson, C., Mebel, A. M., & Kaiser, R. I. 2004, PCCP, 6, 735
Bennett, C. J., Jamieson, C. S., Osamura, Y., & Kaiser, R. I. 2005, ApJ, 624, 1097
Bennett, C. J., & Kaiser, R. I. 2007a, ApJ, 660, 1289
Bennett, C. J., & Kaiser, R. I. 2007b, ApJ, 661, 899
Bergantini, A., Abplanalp, M. J., Pokhilko, P., et al. 2018a, ApJ, 860, 108
Bergantini, A., Góbi, S., Abplanalp, M. J., & Kaiser, R. I. 2018b, ApJ, 852, 70
Bergantini, A., Maksyutenko, P., & Kaiser, R. I. 2017, ApJ, 841, 96
Bernstein, M. P., Sandford, S. A., Allamandola, L. J., Chang, S., & Scharberg, M. A. 1995, ApJ, 454, 327
Bisschop, S. E., Fuchs, G. W., van Dishoeck, E. F., & Linnartz, H. 2007, A&A, 474, 1061
Boogert, A. C. A., Gerakines, P. A., & Whittet, D. C. B. 2015, ARA&A, 53, 541
Brann, M. R., Thompson, R. S., & Sibener, S. J. 2020, JPCC, 124, 7205
Brown, D. W., Florin, R. E., & Wall, L. A. 1962, JPC, 66, 2602
Chaechaty, C., & Marx, R. 1961, JChPh, 58, 787
Charlesby, A. 1965, RPPh, 28, 463
Chou, S.-L., Lin, M.-Y., Huang, T.-P., & Wu, Y.-J. 2020, JMoSt, 1209, 127954
Combes, F., Gerin, M., Wootten, A., et al. 1987, A&A, 180, L13
Cool, T. A., Nakajima, K., Mostefaoui, T. A., et al. 2003, JChPh, 119, 8356
Crovisier, J., Bockelée-Morvan, D., Colom, P., et al. 2004, A&A, 418, 1141
de Marcellus, P., Meinert, C., Myrgorodska, I., et al. 2015, PNAS, 112, 965
Drouin, D., Couture, A. R., Joly, D., et al. 2007, Scanning, 29, 92
Dunning, T. H., Jr. 1989, JChPh, 90, 1007
Eckhardt, A. K., Bergantini, A., Singh, S. K., Schreiner, P. R., & Kaiser, R. I. 2019, AngCh, 58, 5663
Feldman, V. I., Sukhov, F. F., Orlov, A. Y., & Shmakova, N. A. 2001, High Energy Chem., 35, 319
Förstel, M., Bergantini, A., Maksyutenko, P., Góbi, S., & Kaiser, R. I. 2017, ApJ, 845, 83
Förstel, M., Maksyutenko, P., Jones, B. M., et al. 2016, ApJ, 820, 117
Fourikis, N., Sinclair, M., Robinson, B., Godfrey, P., & Brown, R. 1974, AuJPh, 27, 425
Frigge, R., Zhu, C., Turner, A. M., et al. 2018a, ApJ, 862, 84
Frigge, R., Zhu, C., Turner, A. M., et al. 2018b, Chem. Commun., 54, 10152
Frisch, M. J., Trucks, G. W., Schlegel, H. B., et al. 2016, Gaussian 16, Revision A.03 (Wallingford CT: Gaussian Inc.), https://gaussian.com/citation_a03/
Garozzo, M., Fulvio, D., Kanuchova, Z., Palumbo, M. E., & Strazzulla, G. 2010, A&A, 509, A67
Garrod, R. T., Weaver, S. L. W., & Herbst, E. 2008, ApJ, 682, 283
Gerakines, P. A., & Hudson, R. L. 2015, ApJL, 805, L20
Gibb, E., Nummelin, A., Irvine, W. M., Whittet, D. C. B., & Bergman, P. 2000, ApJ, 545, 309
Gibb, E. L., Whittet, D. C. B., Boogert, A. C. A., & Tielens, A. G. G. M. 2004, ApJS, 151, 35
Halfen, D. T., Ilyushin, V., & Ziurys, L. M. 2011, ApJ, 743, 60
Herbst, E. 2014, PCCP, 16, 3344
Herbst, E., Giles, K., & Smith, D. 1990, ApJ, 358, 468

Hollenstein, H., & Günthard, H. H. 1971, AcSpA, 27, 2027
Hollis, J. M., Jewell, P. R., Lovas, F. J., Remijan, A., & Møllendal, H. 2004, ApJL, 610, L21
Holtom, P. D., Bennett, C. J., Osamura, Y., Mason, N. J., & Kaiser, R. I. 2005, ApJ, 626, 940
Hudson, R. L. 2018, PCCP, 20, 5389
Hudson, R. L., & Coleman, F. M. 2019, PCCP, 21, 11284
Hudson, R. L., & Ferrante, R. F. 2019, MNRAS, 492, 283
Hudson, R. L., Loeffler, M. J., & Yocum, K. M. 2017, ApJ, 835, 225
Jacox, M. E. 1982, CP, 69, 407
Jalbout, A. F. 2008, OLEB, 38, 489
Jones, B. M., & Kaiser, R. I. 2013, JPCL, 4, 1965
Jungclaus, G. A., Yuen, G. U., Moore, C. B., & Lawless, J. G. 1976, Metic, 11, 231
Kaiser, R. I., Eich, G., Gabrysch, A., & Roessler, K. 1997, ApJ, 484, 487
Kaiser, R. I., Maity, S., & Jones, B. M. 2014, PCCP, 16, 3399
Kaiser, R. I., & Roessler, K. 1997, ApJ, 475, 144
Kleimeier, N. F., Abplanalp, M. J., Johnson, R. N., et al. 2021a, ApJ, 911, 24
Kleimeier, N. F., Eckhardt, A. K., & Kaiser, R. I. 2020a, ApJ, 901, 84
Kleimeier, N. F., Eckhardt, A. K., & Kaiser, R. I. 2021b, JACS, 143, 14009
Kleimeier, N. F., & Kaiser, R. I. 2021, ChPhC, 22, 1229
Kleimeier, N. F., Eckhardt, A. K., Schreiner, P. R., & Kaiser, R. I. 2020b, Chem, 6, 3385
Kleimeier, N. F., Turner, A. M., Fortenberry, R. C., & Kaiser, R. I. 2020c, ChPhC, 21, 1531
Krim, L., Jonusas, M., Guillemin, J.-C., Yáñez, M., & Lamsabhi, A. M. 2018, PCCP, 20, 19971
Kuan, Y. J., Charnley, S. B., Huang, H. C., Tseng, W. L., & Kisiel, Z. 2003, ApJ, 593, 848
Lacy, J. H., Carr, J. S., Evans, N. J., II, et al. 1991, ApJ, 376, 556
Lee, C., Yang, W., & Parr, R. G. 1988, PhRvB, 37, 785
Maity, S., Kaiser, R. I., & Jones, B. M. 2014a, ApJ, 789, 36
Maity, S., Kaiser, R. I., & Jones, B. M. 2014b, FaDi, 168, 485
Maity, S., Kaiser, R. I., & Jones, B. M. 2015, PCCP, 17, 3081
Matthews, H. E., Friberg, P., & Irvine, W. M. 1985, ApJ, 290, 609
McGuire, B. A., Carroll, P. B., Loomis, R. A., et al. 2016, Sci, 352, 1449
Nummelin, A., Dickens, J. E., Bergman, P., et al. 1998, A&A, 337, 275
Peng, T.-C., Despois, D., Brouillet, N., et al. 2013, A&A, 554, A78
Peterson, K. A., Woon, D. E., & Dunning, T. H., Jr. 1994, JChPh, 100, 7410
Qasim, D., Fedoseev, G., Chuang, K.-J., et al. 2019, A&A, 627, A1
Rachid, M. G., Terwisscha van Scheltinga, J., Koletzki, D., & Linnartz, H. 2020, A&A, 639, A4
Schutte, W. A., & Ehrenfreund, P. 2000, IAUS, 197, 135
Singh, S. K., & Kaiser, R. I. 2021, CPL, 766, 138343
Singh, S. K., Tsai, T.-Y., Sun, B.-J., et al. 2020b, JPCL, 11, 5383
Singh, S. K., La Jeunesse, J., Zhu, C., et al. 2020a, Chem Comm., 56, 15643
Singh, S. K., Vuppuluri, V., Sun, B.-J., et al. 2021, JPCL, 12, 6062
Smaller, B., & Matheson, M. S. 1958, JChPh, 28, 1169
Snyder, L. E., Lovas, F. J., Mehringer, D. M., et al. 2002, ApJ, 578, 245
Swiderek, P., Jäggle, C., Bankmann, D., & Burean, E. 2007, JPCC, 111, 303
Turner, A. M., Abplanalp, M. J., Chen, S. Y., et al. 2015, PCCP, 17, 27281
Turner, A. M., & Kaiser, R. I. 2020, Acc. Chem. Res, 53, 2791
Wall, L. A., Brown, D. W., & Florin, R. R. 1959, JPC, 63, 1762
Wang, J., Yang, B., Cool, T. A., Hansen, N., & Kasper, T. 2008, IJMS, 269, 210
Yang, J. Z., & & Combustion Team 2017, Photonionization Cross Section, & Database (Version 2.0), http://flame.nsrl.ustc.edu.cn/database/
Zhou, Z., Xie, M., Wang, Z., & Qi, F. 2009, RCMS, 23, 3994
Zhu, C., Frigge, R., Turner, A. M., et al. 2018a, Chem Commun., 54, 5716
Zhu, C., Turner, A. M., Abplanalp, M. J., & Kaiser, R. I. 2018b, ApJS, 234, 15